Implicit Geological Modelling of Key Platiniferous Reefs of the Main Chamber of the Bushveld Complex: Implications for the Complex's Structural History

By

Benjamin Stoch

Thesis presented in partial fulfilment of the requirements for the degree Master of Science in Earth Science at the University of Stellenbosch

Supervisor: Dr J.A. Miller

Co-supervisor: Dr I.J. Basson

March 2020

Declaration

I declare that *Implicit Geological Modelling of Key Platiniferous Reefs of the Main Chamber of the Bushveld Complex: Implications for the Complex's Structural History* is my own work, that it has not been submitted for any degree or examination in any other university, and that all the sources I have used or quoted have been indicated and acknowledged by complete references. By submitting this thesis electronically, I declare that the entirety of the work contained therein is my own, original work, that I am the sole author thereof (save to the extent explicitly otherwise stated), that reproduction and publication thereof by Stellenbosch University will not infringe any third party rights and that I have not previously in its entirety or in part submitted it for obtaining any qualification.

Full name: Benjamin Stoch

Date: March 2020

Acknowledgments

The author thanks Dr Ian Basson for supplying the substantial underlying database, as well as his time and expertise during the formulation of this thesis, without which this project would not have been possible. The author thanks the project supervisor, Dr Jodie Miller, for her assistance and insight. The author acknowledges the financial, logistical and software support provided by Tect Geological Consulting. The assistance of Marietjie Schalekamp from the South African Council for Geoscience (CGS), in the sourcing of drillhole data, is acknowledged.

Abstract

The Bushveld Complex (BC) is the world's largest source of platinum group metals and has been extensively studied for decades. The focus of these studies has typically been its geochemistry, magma and PGM genesis, mineral characterization and intrusion mechanisms. Relatively little work been undertaken on the overall 3D geometry of the complex. Without adequate contextualization, analytical results and interpretations from the aforementioned studies may not fully represent the areas within which they were completed, or more subtle trends may not be evident from 2D generic or 3D schematic models. This study aims to offer a broader framework within which these more focused studies may be better contextualized, providing a geological and contextual backdrop to these studies and ongoing research.

This thesis details the construction of 3D implicitly-modelled Merensky and UG2 Reefs across the Rustenburg Layered Series (RLS) of the BC, using open-source and public-domain data. Implicit modelling refers to the mathematical generation of surfaces or solids in 3D space, conditioned to real world data. Multiple data sources, modelling workflows and solutions were explored, to account for the disparities in data resolution, data spacing/clustering, model scale and model output. Modelled features were scrutinised, and anomalous trends or features were identified and subsequently linked to previously-observed or -mapped features. Key outcomes are (1) Construction of a representative, fully implicit, dynamic geological model of the Merensky and UG2 Reefs over the Rustenburg Layered Series of the BC. This bodes well for similar "proof-of-concept" studies over similarly large volumes; (2) Identification of modelled features that may add to the current understanding of the BC's kinematic history and cumulative deformation; and (3) Identification and analysis of subtle geometrical trends and patterns (such as inter-reef spacing and modelled depths), as well as identification of structural domains, which may not have been apparent from numerous, more focussed or isolated petrological/geochemical studies, in model outputs.

Table of Contents

Table of Figures

List of Tables

1. Introduction

The Bushveld Complex (BC) represents the world's largest source of platinum group metals. Although it has been extensively studied for decades, the primary focus of these studies has typically been its geochemistry, magma and PGE genesis, mineral characterization and intrusion mechanisms (Cawthorn and Webb, 2001, 2013; Li, *et al,*, 2001; Webb *et al.*, 2004; Letts *et al.*, 2009). Hundreds of geochemical and petrological studies (published and those produced internally by mining companies), have examined the cumulates layering within individual drillholes or individual sections through mines or exploration projects but have provided very little 3D contextualization across the overall complex. Without adequate contextualization, analytical results and interpretations from the aforementioned studies may not fully represent the areas within which they were completed, or more subtle trends may not be evident from 2D and generic or schematic 3D models. Relatively little work been undertaken on the overall 3D structural geometry of the complex, even though there is a pressing need for this, as noted by Vermaak and Hendriks, 1976; Du Plessis and Kleywegt, 1987; Uken and Watkeys, 1997; Cawthorn and Walraven, 1998; Bamisaiye *et al.*, 2017; Basson, 2019. Construction of a relatively high-resolution 3D model would provide the geological and contextual backdrop to numerous studies, allowing for a more holistic overview of the surrounding geology and ensuring that local and regional geological trends and observations are considered in more local studies and interpretations.

To address this lack of 3D contextualization, this study describes the construction of an implicit 3D model of the historically well-constrained Merensky and UG2 Reefs. Although a vast store of multidisciplinary data has been produced by active mining operations, researchers and exploration enterprises the complex, the vast majority of available academic and industry data remain mineralogical or geochemical in nature, or tightly clustered around economically viable areas over the Eastern, Western and Northern Limbs of the complex. Exploration and mining companies typically seek to delineate or constrain the major platiniferous reefs and marker horizons and publish such open-source information via technical and Competent Person (CP) reports (JORC, NI43-101 and SAMREC). The maps and figures in these reports provided are amenable to georeferencing in a GIS system. Other of data are hard-copy borehole logs, supplied by the South African Council for Geoscience. The implicit model of the UG2 and Merensky Reefs in the Rustenburg Layered Series of the BC, constructed from these data sources, is the first of its kind, in terms of the volume of data and coverage. Furthermore, the model also combines – and benefits from - a multitude of multidisciplinary data sets at different scales: geophysics, geohydrology, structural

geology, igneous petrography, which are combined with geological maps and the abovementioned drillhole logs and maps from the South African Council for Geoscience (CGS).

Given the scale and distribution of available data, this model also serves as a proof of concept demonstration, validating the technical capability of implicit modelling over large volumes, using public-domain data sources. The interpretation of implicitly-modelled features in 3D space, with a backdrop of contextual data and the documented deformational history of the complex, is a novel approach to visualizing the geometry of the Rustenburg Layered Series of the BC.

As surfaces constructed via implicit modelling are mathematically-driven, relative data density and distribution play a greater role in modelling workflow and outcomes, compared to overall data density or data count. In other words, when modelling implicitly, a small area that is densely populated with data is treated the same way as a larger area with scattered data. Carefully managed, implicit modelling is able to produce statistically-relevant and coherent surfaces over large areas or volumes, even if these areas contain data at a variety of scales and densities. The implicitly-modelled Merensky and UG2 Reef surfaces, of the Rustenburg Layered Series, produced in this study are subsequently used as a proxies for the overall 3D geometry of the cumulate pile, thereby providing insight into the deformational history, cumulative strain (e.g. Basson, 2019) and subtle trends in inter-reef thickness and reef dip, such parameters being extracted from the implicit reef surfaces.

It is known that the separation between the Merensky and UG2 reefs varies considerably, depending on the locality within the complex. This separation, derived from the abovementioned implicit 3D model and, in conjunction with reef dip angles, may be used as a proxy to determine the extent of reef deformation. The discussion utilises these deformation proxies to discern areas or zones that have undergone extensive deformation and strain partitioning, expanding our understanding of the BC's kinematic history. These deformation proxies do not assume horizontal layering, but rather represent a relative scale of deformation determined versus background values. For example, areas that have undergone extensive deformation may display greater inter reef separation/dip/depth than adjacent areas, so a relative scale is used to compare them

The implicitly - projected or -inferred positions of modelled Merensky and UG2 Reefs will, moreover, provide useful references and targets for future exploration programs. Therefore, the primary aim(s) of this thesis is to

create a proof of concept model (can it be done at this scale and as well as provide robust outputs for analysis), investigate/interrogate modelled surfaces, and to explore the further theoretical and practical applications of the model.

1.1 Summarised Objectives:

To achieve the primary aim(s) of this study, the following specific objectives and key questions have been identified and addressed:

1. To construct 3D, implicitly-modelled surfaces, representing the Merensky and UG2 Reefs, across the Rustenburg Layered Series of the Bushveld Complex, using open-source and public-domain data. *Inter alia*, the following questions will be addressed:
    a. What is the data resolution required to construct a representative geological model?
    b. How are data resolution disparities resolved in the model?
    c. What is the best method of evaluating the adopted modelling technique and whether or not this produces a most robust geometry?
2. To establish the relative confidence or uncertainty in the geological model:
    a. What is an appropriate methodology for evaluating uncertainty?
    b. Establishing or highlighting areas of relatively high or low confidence;
3. To identify patterns and domains in the modelling products that relate to deformation, utilizing modelled marker reefs, inter reef separation (middling) and reef dip as deformation proxies:
    a. Does the model facilitate the identification of trends in inter-reef thickness and reef dip?
    b. Establish which modelled areas/features are related to known deformation features or events;
    c. How do these deformation proxies relate to our current understanding of the kinematic history or cumulative strain of the Bushveld Complex?

1.2 Thesis Outline

The thesis is comprised of 7 sections, and it is anticipated that sections 4-8 will be summarized and formatted to meet the required standard of an international journal publication.

Section 2: An extended background and literature review of topics relevant to the thesis. Specifically, the section introduces the reader to the regional geological and tectonostratigraphic history of the BC, and further expands on historical conceptual models related to the BC, its deformation and emplacement.

Section 3: An overview of both geomodelling theory and modelling methodology utilised for the construction of the BC reef model. This section further discusses the value in establishment of a relevant structural framework, prior to model construction.

Section 4: A description of the model construction procedure, detailing relevant modelling parameters such as choice of model extent, data import and validation. This section presents a methodology to address disparities in data resolution and reliability.

Section 5: Provides an introduction into modelling uncertainty, the manner in which it is evaluated, and its applicability to the BC geological model.

Section 6: Overview of modelling results, summarised and referring to a series of figures

Sections 7-8: Discussion and Conclusions. These sections illustrate the utility of the inter-reef spacing between modelled reefs and their dip angles as proxies for deformation. The last point, conveyed in this section, concerns the overall structural interpretation and kinematic implications on a regional scale and assesses their implications to real-world outcrops and mines. The final section summarizes the key finding of the thesis and also provides further recommendations that will be of benefit to future modelling or refinement of the BC reef model.

2 Geological Setting and Historical Modelling

2.1 Geological Context

The BC is the world's largest layered intrusion, with an estimated average thickness between 7 – 9 km, and an original regional coverage of over >100 000 km^2 (Uken 1998; Eales and Cawthorn, 1996; Cawthorn *et al.*, 2012). More importantly, the BC represents the largest known concentration of Cr and Platinum Group Metals (PGM) globally (Du Plessis and Walraven, 1990). The complex consists of four major limbs: Northern, Southern, Eastern, Western (including the Far Western) Limb and the far Northern Villa Nora Complex or fragment (Figure 1). Contemporary thinking suggests that the complex was emplaced as a series of broadly flat sheets or protrusions, with the main body of the igneous complex intruding into Proterozoic Pretoria Group sediments (Kruger, 2005; Clarke *et al.*, 2009), with present day outcrops covering an area in excess of 65 000 km^2 (Cawthorn *et al.*, 2006; Lenhardt and Eriksson, 2012; Figures 1 and 2).

The BC is comprised of the following primary components: the predominantly felsic Rooiberg Group extrusives (2061 ± 2 Ma; Walraven, 1997); an ultramafic-mafic Rustenburg Layered Suite, (2058.9 ± 0.8 Ma; Buick *et al.,* 2001), the Lebowa Granite Suite (2054 ± 2 Ma; Walraven and Hattingh, 1993), and the Rashoop Granophyre Suite (2053 ± 12 Ma; Coetzee and Twist, 1989; Figure 1). Emplacement of layered main body of the complex (RLS) was preceded by the extrusion of the relatively undeformed and unmetamorphosed Rooiberg Group (Lenhardt and Eriksson, 2012), the latest component of the Transvaal Supergroup (Eales *et al.*, 1993; Eales and Cawthorn, 1996). The Rooiberg Group is petrogenetically related to the larger Bushveld magmatic event (Lenhardt and Eriksson, 2012), described in numerous studies on the age and crystallization time of BC magma (e.g. Eriksson and Reczko, 1995; Lenhardt and Eriksson, 2012; Cawthorn *et al.*, 2012; Zeh *et al.*, 2015). The ultramafic-mafic sequence of the RLS is further compositionally subdivided into five zones (Cawthorn *et al.*, 2006) including several marker horizons (summarised in Figure 2), based primarily on observations and data from the Eastern and Western Limbs (Eales and Cawthorn, 1996). These zones, grading from the base of the RLS, are the Marginal, Lower, Critical, Main and Upper Zones.

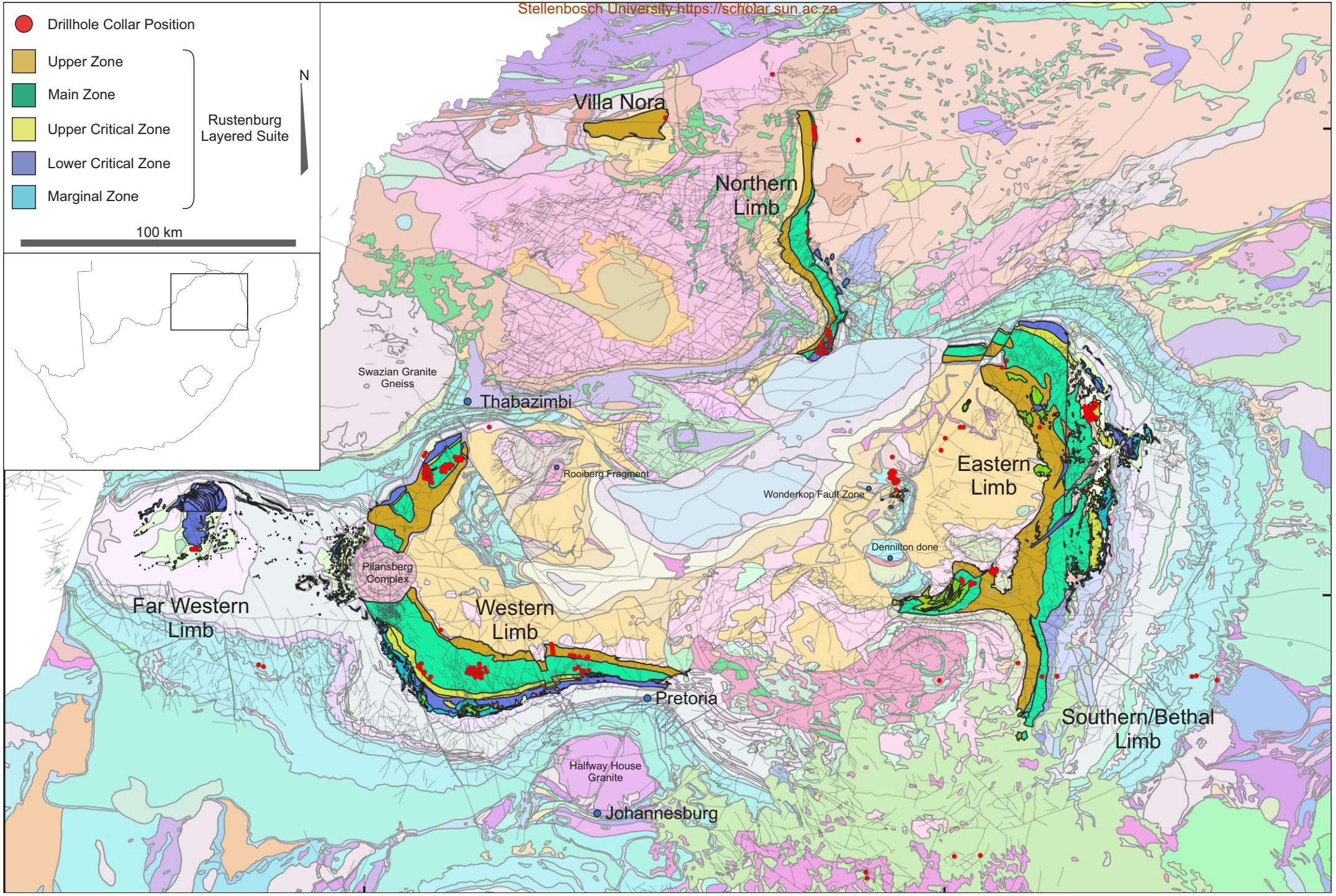

Figure 1: Overview of the Bushveld Complex, indicating the position of the primary limbs: Northern, Southern, Eastern and Western. Positions and lithologies provided by the open-source Council for Geosciences' (CGS) ArcMap project, which indicate the position and distribution of the Rustenburg Layered Suite. The legend is detailed in Figure 2. Collar positions of open source drillhole data are shown.

Era	Supergroup	Group	Sub-group	Formation
Mesozoic	Karoo			Lebata
				Clarens
				Irrigasie
Palaeozoic		Ecca		
		Dwyka		
Mokolian		Waterberg	Kransberg	Vaalwater
				Claremont
				Sandriviersberg
				Mogalakwena
			Metlabas	Makgabeng
				Skilpadkop
				Setlaole
			Nylstroom	Alma
				Swaershoek
				Wilger River
				Blouberg
Vaalian				Loskop
				Rus de Vinter
				Glentig
	Traansvaal 2.5– 2.06 Ga	Rooiberg (2061 ± 2 Ma)		Selons River
				Schkrikkkloof
				Kwaggasnek
				Rinkhalskop
				Smelterskop
		Bushveld Complex	2054 ± 2 Ma (2061 ± 2 Ma)	Lebowa Granite Suite
			2058.9 ± 0.8 Ma (2061 ± 2 Ma)	Rustenberg Layered Suite
				Schilpandnes
			2053 ± 12 Ma (2061 ± 2 Ma)	Rashoop Granophyre Suite
		Pretoria		Salie Sloot
				Leeuwpoort
				Steenkamsberg
				Kwarriehoek
				Rayton
				Magaliesberg
				Silverton
				Daspoort
				Strubenkop
				Hekpoort
				Timeball Hill
		Chuniespoort		
		Black Reef		
Randian		Wachteenbeetjie		
		Buffelsfontrin		
		Bloemfontein		

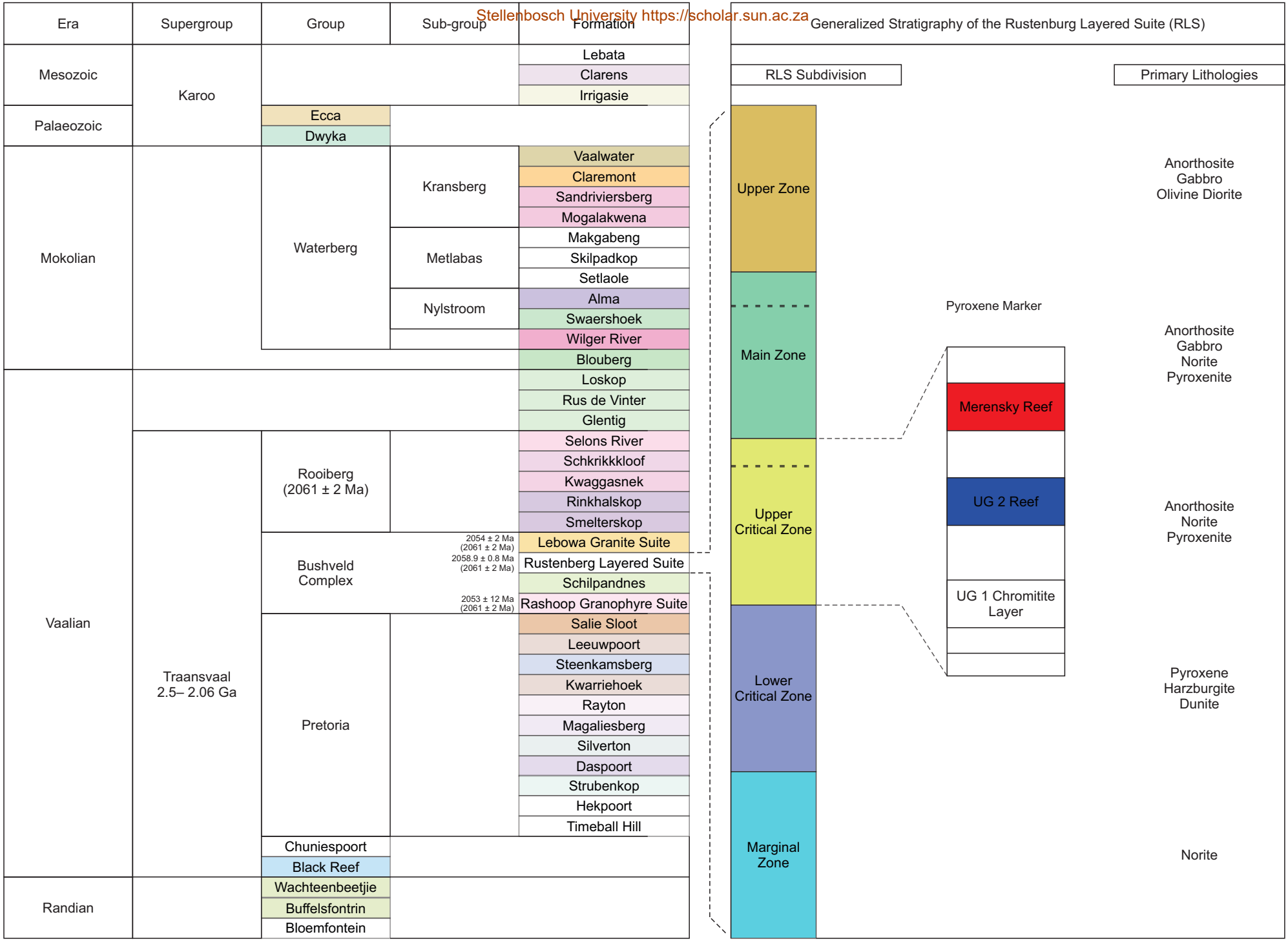

Figure 2: a) Table summarizing the Karoo Supergroup, Transvaal Supergroup, Waterberg Group, and older basement units. The accompanying legend applies to all subsequent figures. b) Simplified or typical vertical section through the Eastern and Western Limbs, showing position of Merensky and UG 2 reefs, modelled in this contribution.

The Marginal Zone is typically composed of gabbronorite/norite and minor meta-sediments (Vermaak and Hendriks, 1976; Kruger, 2005), with typical thicknesses seldom exceeding 250 m. This zone has been interpreted as a widespread chill zone that defines the base of the complex (Eales *et al.*, 1993; Kruger, 2005), given the lack of exposure, it is interpreted that this zone transgresses up along (bounding) the Lower-Critical Zones. The lower zone consists primarily of accumulated (starting at the base) chromite, dunite, harzburgite to pyroxenite, with small amounts of intercumulus plagioclase, secondary biotite and clinopyroxene, displaying variable thicknesses (Boorman *et al.*, 2004; Cawthorn *et al.*, 2006) of cumulate pyroxenites and olivine enriched constituents (Viljoen and Schurmann, 1998). Chromitites are typically absent, except in portions of the Northern Limb (Hulbert, 1982).

The Critical Zone is between 1 300 m and 1 800 m thick (Naldrett *et al.*, 2008) and bounded by first occurrence of cumulus chromite bands, marking the base of the Critical Zone, whilst the Giant Mottled (poikilitic) Anorthosite, positioned many meters above the well-documented and highly economic Merensky Reef, represents the Critical Zone's top contact. It is characterized by the regular layering of chromitites, pyroxenites, dunites and harzburgites (Eales *et al.*, 1993). The Critical Zone is further subdivided into the Upper Critical Zone (UCZ) and Lower Critical Zone (LCZ, see inset on Figure 2) (Vermaak and Hendriks, 1976; Seabrook *et al.*, 2005; Eales and Cawthorn, 1996; Cawthorn *et al.*, 2006; Eales and Costin, 2012). Pyroxenite, harzburgite and chromite make up the bulk of the Lower Critical Zone, while the Upper Critical Zone (UCZ) contains chromite, feldspathic pyroxenite, norite and anorthosite/troctolite layers (Kruger, 2005; Mondal and Mathez, 2007).

The UCZ consists of thick anorthosite and noritic anorthosite, with intercalated pyroxenite units and chromite reefs that are remarkably regular in mineralogy and thickness, with regards to cyclical units and their lateral continuity (Cameron, 1977). The UCZ displays well-defined layering, exhibits extraordinary enrichment in PGE's and chromite (Cawthorn *et al.*, 2006) and represent 50% and 75% of the world's Pd and Pt resource, respectively (Cawthorn, 1999; Seabrook *et al.,* 2005). Given this mineral endowment of these two reefs within the CZ, and even though the CZ represents only a relatively small part of the BC, it has been the primary focus of most research and analysis across the BC.

The Main Zone (MZ), whilst not distinctly layered, does contain repetitive cumulate layers of pyroxenite, anorthosite and norite/gabbronorite, with two distinct marker layers, the Pyroxenite Marker and the Main and Upper Mottled Anorthosite, being noteworthy (Eales and Cawthorn, 1996). Upper Zone (UZ) gabbronorite and anorthosite, with cumulus Fe-rich pyroxenes, olivine, magnetite and apatite, contains numerous V-bearing

(Cawthorn *et al.*, 2006) magnetitite stringers, subdivided into four groups of up to seven layers each (Eales and Cawthorn, 1996). Erikson et al (1995) noted that the upper Pretoria Group is intruded or cross-cut by the RLS which has effectively lifted the Rooiberg Suite to form the complex's canopy, with the later Lebowa and Rashoop Suite granites later intruding the upper portions of the RLS and Rooiberg felsites (Eriksson *et al.*, 1995). BC's 4 zones are thought to become more extensive up through the RLS, with the MZ is inferred to extend 450 km east-west and 350 km north-south (Naldrett *et al.*, 2008). The eastern and western limbs of the RLS dip towards its centre at 10°-20° (Cawthorn and Webb, 2001). This dip has been attributed to isostatic adjustment of the crust in response to the large density contrast between mafic units (± 3.02 g/cm^3) of the BC and the surrounding host units (±2.6 g/cm^3), (Cawthorn and Webb, 2001; Webb *et al.*, 2004; Cawthorn, 2013).

Despite its age (2055 Ma), the complex is generally not thought to have undergone any significant metamorphism or deformation other than the mentioned apparent tectonic subsidence (Eales and Cawthorn, 1996; Cawthorn and Webb, 2001). However, this has been challenged by Basson (2019), who suggests that deformation of the deeper, central portion of the Rustenburg Layered Series was responsible for fluid expulsion and generation of (1) Transvaalide fold and thrust event, (2) intrusion of a High-Titanium Suite of intrusions (HITIS) and (3) anticlockwise rotation of the eastern 2/3^{rds} of the Rustenburg Layered Series. Although separated by a significant amount of cover rocks, the Western and Eastern Limbs are likely interconnected at dept, given their remarkable similarity in their composition, consistency in layering and geochemical signatures (Cawthorn and Webb, 2001; Webb *et al.*, 2004; McCall, 2016).

Both the Merensky and the UG2 reefs formed as distinct, persistent layers within the RLS of the BC (i.e., its western and eastern lobes as well as partially into its norther limb). The Merensky Reef, wherein much of the PGE mineralization associated with the complex is hosted, predominantly consists of a coarse-grained pegmatoidal feldspathic pyroxenite that contain appreciable phlogopitic mica. The Merensky varies in thickness from 15 cm to 40 cm, with upper and lower contacts of coarse-grained material typically marked by thin chromitite layers several millimetres thick. Immediately above the top chromitite layer is a brownish pyroxenite, known as the Merensky Pyroxenite, with an average thickness of 60 cm (Cawthorn and Webb, 2001). As platinum minerals occur both within and in association with pyroxenite sulphides, the Merensky Reef yields substantial copper and nickel as by-products, together with minor amounts of cobalt and selenium. In the Eastern Limb, the

Merensky Reef is also well developed but may not be pegmatoidal, or if pegmatiodal, may be virtually barren. In the Western Limb, a pegmatoidal phase is strongly developed, as are its chromitite contact layers.

Regionally, the UG2 is a platiniferous chromitite reef that ranges in thickness from 0.4 m to 2.5 m, although occurrences greater than >2.5 m are occasionally observed. This package typically comprises 2 – 9 chromitite layers, intercalated with melanocratic host material that contains a thin chromitite leader (Voordouw *et al.,* 2010). The footwall of the UG2 typically comprises either anorthositic rock or pegmatoidal pyroxenite (Cawthorn, 2017), with the hangingwall materials differing between the eastern and western limbs: the western limb hangingwall typically comprising of an olivine enriched pyroxenite, while the eastern limb is predominantly overlain by pyroxenite (Cawthorn, 2017). The UG2 Reef package has an average chromite content of 30 – 35 % (Schouwsta *et al.*, 2000), although individual layers of chromitite range in chromitite concentration up to 90 % chromite (Mathez and Mey, 2005). The majority of PGE minerals are associated with base metal sulphides, predominantly chalcopyrite, pyrrhotite and pentlandite, and silicates. The position of the UG2 within the cumulate pile is somewhat erratic, varying between 15 m and 400 m below the Merensky Reef (Schouwstra *et al.,* 2000; Cawthorn, 2011).

2.2 Conceptual Models: Connectivity Between Eastern and Western limbs

The Eastern and Western Limbs show marked similarities, despite the great distance (in excess of 150 km) between their outcrops. The connectivity between these limbs has been extensively discussed (Cousins, 1959; Cawthorn and Webb, 2001; Webb *et al.*, 2004; Cole *et al.,* , 2013; Finn *et al.*, 2015; McCall, 2016). Their similarities and connectivity are summarised by Webb *et al.* (2004) as follows:

1. Four layers of Middle Group chromitites with plagioclase becoming a cumulus phase above the second layer;
2. A bifurcating and deformed footwall of the UG1 chromitite;
3. Economic grades of PGE mineralization of the UG2 chromitite;
4. A sharp stratigraphic break in the initial Sr isotopic ratio at the Merensky Reef;
5. All zones have identical initial Sr isotopic ratios; and
6. Similar thicknesses and grades of the Main Magnetite Layers in the Upper Zone.

Petrological, geochemical and isotopic characteristics are therefore suggestive of interconnectivity between the Eastern and Western Limbs (Webb *et al*., 2004). Distribution of intermittent exposures of mafic materials, believed to be associated with the BC, indicate the possibility that the complex is more developed or preserved in the centre of the two limbs in some format. As a result, a wide range of models have been developed for the complex, each revolving around various degrees and modes of limb interconnectivity (Cole *et al.*, 2014).

Parts of the regional 3D geometry of the Bushveld Complex has been extensively researched and debated (Hall, 1932; Coetzee and Twist, 1989; Uken and Watkeys, 1997; Gerya *et al.*, 2003; Webb *et al.*, 2004; Clarke, Uken and Reinhardt, 2009; Cole, Finn and Webb, 2013; Finn *et al.*, 2015). This is in parts limited by a relatively limited distribution of outcrop, a paucity of information at depth - particularly in the central region of the Rustenburg Layered Series - and the overall scale of the BC. Despite these challenges, several geometry models have been proposed. An initial lopolithic geometry was proposed by Hall (1932) and du Toit (1954), based on the availability of outcrop and general understanding of the BC at the time. This initial interpretation fell out of favour, primarily due to work by (Cousins, 1959), wherein the Bouguer gravity anomaly in the central portion of the Bushveld Complex was cited as being similar to background values outside of the Complex. In other words, if lopolithic, the Bouguer gravity value in the central portion would be elevated relative to this background value.

Discussions on the continuity and geometry towards the central portion of the Rustenburg Layered Series were hampered by the lack of deep drillholes and consequently rely on scattered information from non-PGE/Cr mines and geophysical data inversion (Basson, 2019). For instance, the two separate dipping sheets model, proposed by Cousins (1959), was initially supported by the lack of RLS distribution at depth and the lack of RLS outcrop between the two main limbs. The same study (Cousins, 1959) interpreted intrusions with separate vertical feeders (see also Viljoen, 1999), such as those that may emanate from the edges of a mantle diapir penetrating the crust. Older gravimetric studies and geoelectric surveys (Du Plessis and Kleywegt, 1987; Meyer and de Beer, 1987) indicated the lack of mafic units between the Dennilton Dome and the Rooiberg Fragment (Figure 1). Additional geophysical work completed by (Cheney and Twist, 1991) supported an absence of RLS at depth, between the Eastern and Western Limbs. Models that were based on individual, inward-dipping sheets and the concept of discrete or separate limbs were presented by several authors (Molyneux and Klinkert, 1978; Sharpe and Snyman, 1980; Du Plessis and Kleywegt, 1987; Meyer and de Beer, 1987).

In contrast, more recent studies support greater inter-limb continuity at depth (Cawthorn and Walraven, 1998; Cawthorn and Webb, 2001; Webb *et al.*, 2004; Webb, Ashwal and Cawthorn, 2011). Work by Cawthorn and Webb (2001) support the idea that the development of Bushveld mafic units was intermittent at the very least between the Eastern and Western Limbs. Aeromagnetic modelling by Cole *et al.* (2013) indicates a significant volume of BC material between the Eastern and Western Limbs, and west of the Wonderkop and Stofpoort Faults (fault positions indicated in Figure 3), as well as supporting the concept of continuous mafic rocks between the western and eastern lobes. Cole *et al.*, (2013) also note that aeromagnetic anomalies of the RLS is heavily influenced by the magnetite-rich UZ materials, which result in the majority of discernible positive magnetic anomalies and layering previously mentioned.

When referring to emplacement mechanisms, intrusion of a relatively flat sill into a broadly folded basin was proposed by (Gruenewaldt, 1979), while (Eales *et al.*, 1993) surmised that these sheets were initially emplaced horizontally. Structural studies are focussed primarily along the northern margin of the complex, in mines on the southern part of the Western Limb, in fragments and around domes; as a result, the majority of the complex is poorly documented from a structural standpoint. Notwithstanding this, work by Kinnaird and McDonald (2005) and Kinnaird *et al.* (2017) indicate that the NL is most likely detached from the main part of the BC chamber by the ENE trending Thabazimbi Murchison Lineament (TML), which may have comprised a dyke-like feeder for magmas, resulting in an impediment between the Northern Limb and the main body of the complex (Kinnaird *et al.,* 2017). Gravity models by Finn *et al.* (2015), furthermore, indicate moderately thicker and/or high-density materials at fault intersections - within the western and central TML- interpreted as feeders, although this interpretation relies on the assumption that the extent of deformation in these areas is limited. Kinnaird *et al.,* (2017) suggests that there may be multiple sub-chambers within the BC, wherein intrusion and crystallization of the cumulate pile was distinct from the remainder of the complex, and that this may be present within a single limb.

Essentially, and in summary, there are four primary geometry models currently circulating:

1) The Eastern and Western limbs are separate or discrete (Cousins, 1959);

2) The complex is continuous at depth: the connected lobes model (Cawthorn and Walraven, 1998; Cawthorn and Webb, 2001; Webb *et al.*, 2004; Cole, Webb and Finn, 2014);

3) The complex is predominantly continuous, with locally disruption by major structures or domes: the separate dipping sheets model (Du Plessis and Kleywegt, 1987; Meyer and de Beer, 1987);

4) The central part of the Rustenburg Layered Series has been extensively displaced by thrusting southwards, the eastern and western limbs at depth have also undergone a degree of thrusting and folding and the eastern 2/3^{rds} of the Rustenburg Layered Series has been rotated by approximately 35° anticlockwise (Basson, 2019). Effectively, Basson (2019) proposes that we cannot assume that the current geometry of the BC to reflect the "original" complex.

3 Modelling Methodology

3.1 Geomodelling Theory

The mining industry utilizes two primary methodologies for 3D geomodelling: explicit (sometimes termed geometric) and implicit (Vollgger *et al.*, 2015; Stoch *et al.*, 2017). Explicit modelling is inherited from computer-aided design (CAD) drafting software, which initially replaced manual drafting. In the geomodelling industry, this explicit methodology relies on the manual construction of interpretations on 2D vertical cross-sections and/or surface maps (Cowan *et al.*, 2003; Cowan *et al.,* 2011; Vollgger *et al.*, 2012), typically by applying software packages such as Geovia's GEMS, AutoCAD, SURPAC and Datamine.

Explicit modelling requires manual digitization across pre-determined, multi-sectional views, which are effectively interpreted, usually across-strike, and often simplified cross-sections. Manual digitization across cross-sectional interpretations are linked along strike to generate surfaces, such as a contact and/or fault planes, or solids in the case of lithology-defining closed polylines. The manner in which interpreted polylines are linked is strongly influenced by many factors (Cowan *et al.*, 2003; Cowan *et al.,* 2011; Vollgger *et al.*, 2013), for instance, data density, geological complexity and even the orientation of the modselling sections strongly influence the sresultant modelled geometries (Stoch *et al.*, 2017). Manual digitization of cross-sections and wireframe construction is typically results in significant simplification of interpreted lithological contacts and constructed wireframes in an attempt to complete modelling procedures in a timeous manner (Cowan *et al.,* 2011; Lindsay *et al.*, 2012; Vollgger *et al.*, 2015). These simplified interpretations are typically non-representative of the geology or structural complexity of the systems being modelled (Caumon *et al.*, 2013; Vollgger *et al.*, 2015). Wireframe simplification is particularly apparent when the user views secstions that are at high angles to those used for model construction or along-strike sections. These almost inevitably generate geologically-unrealistic surfaces and volumes in areas hosting complex geology.

Implicit modelling refers to the production of function-derived surfaces, with the most widely-used function in 3D geomodelling being the radial basis function (RBF, Vollgger *et al.*, 2015). The development of implicit modelling in the mining industry, summarized in Cowan *et al.* (2002), culminated in the development of rapid geological modelling in Leapfrog™, a software package that utilizes rapid interpolation (mathematical term, denoting the generation of an intermediate value into a series by calculating it from surrounding known values), functions to generate 3D geometries (Cowen *et al.*, 2003; Vollgger *et al.*, 2015; Stoch *et al.,* 2017). Modelled

surfaces produced via implicit modelling represent the iso-potentials of a scalar field in 3D space (Bloomenthal and Wyvill, 1997; Caumon *et al.*, 2013; Vollgger *et al.*, 2015). A scalar field is the grouping of representative numerical values with their positions in 3D space, and these numerical values may be derived from both numeric and non-numeric data. Simply put, surfaces modelled utilizing implicit functions represent the *regions* in 3D space that show the highest likelihood (or potential) for surface position and shape, interpolated between hard data points such as drillhole contacts.

Lithological data and other non-numeric data are converted to a representative scalar value, for example these scalar values may represent assay values, fault intersections or distance to lithological contacts (Carr *et al.*, 2001; Cowan *et al.*, 2003; Caumon *et al.*, 2013; Vollgger *et al.*, 2015). These values are interpolated, resulting in an isosurfaces that may be groomed to intersect original data points (e.g. lithological contacts, fault intersections). These scalar values may be locally adjusted or weighted according to available planar structural data, as described by Hillier, *et al.,* (2013). This allows modelled surfaces to defer to – or benefit from - structural trends (Caumon *et al.*, 2013; Vollgger *et al.*, 2015). The advantages of this are as follows:

1. Modelled surfaces may be modified locally with hard data;
2. Surfaces may be adjusted by user-defined orientation values, in *lieu* of available data (Stoch *et al.*, 2017);
3. Directional bias, inherent in section-based explicit modelling, is removed or absolutely minimized;
4. Extrapolation away from known or hard data, into areas where there is effectively no data, may be done intelligently, using trends;

Implicitly-modelled surfaces (prior to Boolean clipping functions) show smooth and usually geologically-realistic geometries. An additional advantage of implicit modelling is the negation of *ad-hoc* rules during digitization and assembly of lithologies, which may be abused in cases where there is complex lithological logging or where the geologist undertaking the modelling does not fully understand the overall geological context.

Implicit modelling is not, however, without limitations. Multiple, mathematically-induced artefacts have been noted. An example of one these artefacts is over-simplification of modelled surfaces in areas of low data density, as the RBF will attempt to snap to control points, which consequently may not generate representative surfaces where geological or structural abruptly terminate against tectonostratigraphic features. Additionally, RBF

surfaces and solids near model boundaries may expand exponentially away from data, termed “ballooning”, towards and into areas of little or no hard drillhole data or other guiding input (Fornberg *et al.*, 2002; Driscoll and Heryudono, 2007). Jessell *et al.*, (2014) noted that local data density has a greater influence on the resultant surfaces produced, rather than the specific RBF employed. Noticeable differences between these techniques are typically mitigated by high data density. For this study, Leapfrog Geo V4.5 rules-based implicit modelling software was utilized for 3D model construction.

3.2 Methods

Rules-based or conditional modelling is the automated application of user-defined conditions to a dataset. These conditions are dependent on the modelling software, workflow, model application and underlying data. In the case of 3D geomodelling in Leapfrog Geo, this procedure follows a standardized workflow (Figure 3):

1. Establishment of a volume of interest (VOI);
2. Incorporation of data;
3. Subdivision of the VOI into structural domains;
4. Subdivision of structural domains into geological units/volumes;
5. Analysis and modification of resultant geological units/volumes.

The subdivision of the VOI, structural domains and final lithological volumes requires unique data points. For example, in the case of interpolated contacts, these represent lithological, structural, geochemical or any user-defined boundaries. Each interpolated contact surface describes or represents user-defined, interpolated scalar values that vary within the VOI (Carr *et al.*, 2001; Cowan *et al.*, 2003). These interpolated contact surfaces represent the calculated “best-fit” curves between available data points, given user-defined search criteria (Cowan *et al.*, 2003).

Geological features, such as contact points, contact conditions and way-up directions, are established as series of guiding assembly rules that are geologically-phrased and geologically-logical. An example of this is the establishment of a chronological sequence (Figure 3), dictating how the stratigraphic or tectonostratigraphic sequence should be assembled. This is accomplished by specifying age and contact relationships, as well as younging directions and cross-cutting relationships or chronology of the various interpolated surfaces. Once the contacting and age relationships between surfaces are defined, geological parameters are established per

contact surface. Geological features may be modified according to observed deformation style(s) and structural trends may be incorporated with a number of surface construction tools (e.g. anisotropic ellipsoid trends or roaming structural trends), which allow for greater surface control and the generation of geologically-realistic output surface geometries.

The resultant contact surface is a visual representation of a mathematical "best-fit" curve in 3D space that obeys both hard positional data and a series of imposed rules (Stoch *et al.*, 2017). Once these contact surfaces have been used to subdivide the VOI into its various subdomains and lithological solids, the contact surfaces are amenable to iterative interrogation or inspection, adjustment of parameters or rules and subsequent modification by the insertion of explicit controls. Once an appropriate contact surface is established, it is then activated to subdivide the model and to subsequently enable the export of industry-standard wireframes or triangulations. The workflow developed for the implicit BC Rustenburg Layered Series reef model is detailed in the following chapters.

Data collation
Selection of coordinate system
Import and QA/QC of data into a single coordinate system
Generation of the Volume of Interest

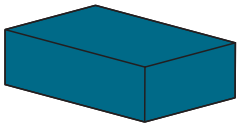

Structural interpretation based on available data
Generation of initial structural network

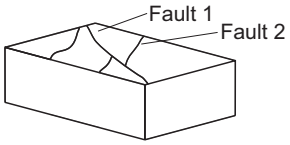

Activation of faults to structurally domain model
Review of data/literature per structural domain
Establishment of surface chronology

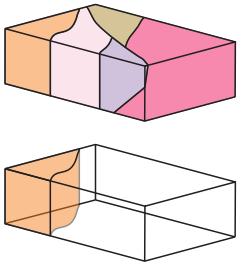

Development of surface chronologies per structural domain
Establishment of cross-cutting and chronological relationships of geological units

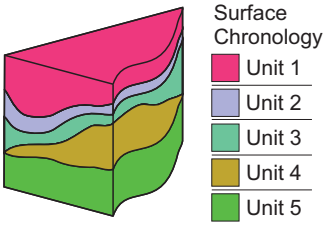

Activation of geological units
Subdivision of structural domains into geological volumes
Finalization of volumes, QA/QC of volumes

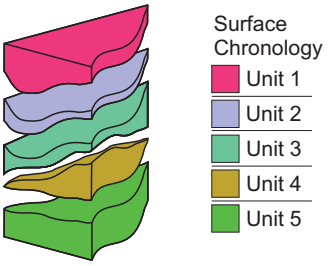

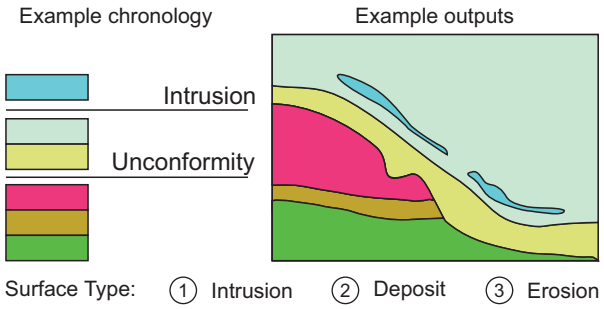

Figure 3) Schematic of typical rules-based conditional modelling. Leapfrog has three primary methods or functions for surface and volume construction.

The intrusion function produces an enclosed volume, from a boundary determined by “inner” and “outer” contacts, derived from a series of intervals.
The deposit function results in a single contact surface, which when activated, will result in a series of conformable, chronologically-ordered volumes.

The erosion function generated a contact surface, which cross-cuts and removes lithological volumes that are considered more recent in the modelling chronology.

3.3 Structural Interpretation

A core component of 3D geomodelling is the early establishment of a representative conceptual structural network (Masse and Laurent, 2016; Stoch *et al.*, 2017). The conceptual structural network is used to discretize the modelling volume into fault domains. This discretization effectively delineates structurally-bound subdomains, within the VOI, which have – or appear to have, based on the available data - undergone similar deformation histories. This delineation ensures that surfaces within the same structural domain share equivalent structural trends and/or modelling controls. Key structures and other features were selected from the structural framework of Basson (2019). Table 1 summarises these digitized features.

Features	Number (Point/Line Segments)
Faults	10 130
Fold Axes	184
Tectonic Fabric	25 722
Orientation/Mapping Data	5 396
IRUPs and Dunite pipes	3 189
UG2 and Merensky Reef Contours	868

Table 1: Summary of data compiled by Basson (2019) and supplied to the author in GIS compatible formats. These datasets underwent digitization, re-evaluation, selection and incorporation into the 3D modelling environment.

The South African Council for Geoscience released a vector map that delineates the regional geology of South Africa, as well as incorporates several major structures. This vector map, combined with selected components derived from the Molyneux (2008) digital compilation, was used as a contextual lithological backdrop to Basson's (2019) structural interpretations. The compiled fault network and available structural readings were imported from ArcGIS into the Leapfrog modelling environment as a series of shapefiles. Fault delineation and construction incorporates various field mapping, geophysical and stratigraphic/drillhole datasets. A total of 63 faults, based predominantly on those interpreted by Basson (2019), were assembled into a cohesive fault network from the total of 10 130 fault segments, re-constructed in Leapfrog Geo, and explicitly characterized in terms of their crosscutting chronological order. Several of these faults were designated as domain-bounding structures, effectively encompassing or ringfencing an individual sub-model (Figure 4).

4 Conceptual Model Construction

My BC model construction followed a standardized workflow, however, additional provisions made to address specific modelling requirements to construct the UG2 and Merensky Reefs. The following section reports the various modelling requirements, parameters and provisos.

4.1 Establishment of Volume of Interest

The VOI (Figure 3) encompasses the bulk of public-domain data across the Rustenburg Layered Series of the BC, with its eastern, western and southern margins defined by a buffer region of 500 m outwards from surface UG2 and Merensky Reef outcrops (Figure 5).

The eastern, western and southern margins were derived by merging surface reef traces in a 2D environment (QGIS, build Girona 3.2) and constructing a buffer region around these traces, which was manually edited and dissolved to provide individual, but continuous, outlines for modelling VOI, within each limb. The VOI encompasses a total volume of approximately 270 000 km^3, with a lateral extent of approximately 400 km by 330 km and a modelled depth of approximately 6 km below a static maximum height (base of model set to - 4 500 MASL).

The VOI's northern extent is a 500 m buffer, northwards of structures interpreted to form part of the Thabazimbi–Murchison Lineament (TML) or fault system (Good and de Wit, 1997; Basson, 2019). The TML is a well-documented, regional tectonic boundary which, along with the Mohlapitsi Fold-and-Thrust Belt, the Welgevonden/Southern Fault System and the Zebedelia Fault, trends ENE-WSW, for approximately 600 km, across the Kaapvaal Craton, representing a broad, regional shear zone that was active syn- to post-BC emplacement (Cheney and Twist, 1991; Good and de Wit, 1997; Basson, 2019). The TML effectively seperates the Northern Limb from the Rustenburg Layered Series of the BC (see also Kinnaird *et al.*, 2017), and is utilized in my model as a natural boundary for the VOI's northern extent.

500 000 600 000 700 000 800 000

7 350 000

7 200 000

Legend

- Drillhole Collars
- Merensky Reef Outcrop
- UG2 Outcrop
- MG Chromitites
- LG Chromitites
- Magnetite Reefs
- Other Reef Outcrop
- Digitized Reef Contours
- Key Faults
- Key Dykes
- Faults
- Gravity Inversion Contours
- Volume of Interest
- Ultramafic Pegmatoids

100 km

N

Northern Limb

Eastern Limb

Western Limb

Southern/Bethal Limb

Pilansberg Complex

Ysterberg Planknek Fault

Strydpoort Fault

Stofpoort Fault

Zebedilia Fault

Welgevonden/Southern Fault

Wonderkop Splay

Dwarsrivier Fault

Thabazimbi–Murchison

Eilandsberg Fault

Warmbaths Fault

Southern Boundary Fault

Droogekloof Thrust

Southern boundary Fault

Wonderkop Fault Zone

Brits Graben Fault

Crocodile River Fault

Brits Graben Spray

Marikana fault

Rustenburg Fault

Steelport Fault

Laersdrift Fault

Rietfontein Fault

Figure 4: Boundary of VOI and data distribution. The primary datasets employed in this project are detailed in Appendices 1-4. Notable features include: 1) north-up reverse faulting along the TML, Zebediela, Welgevonden/Southern, Bobejaanswater Fault systems; 2) SSE-directed thrusting in the Droogekloof Thrust, Boschpoort Fault/ Thrust and Southern Boundary Fault system; 3) lack of dome development within the WL.

The central and northern areas of the BC Rustenburg Layered Series are largely obscured by sediments of the Waterberg and Karoo Supergroups, with few identifiable Bushveld Complex outcrops or occurrences noted. The geological model presented herein is constructed in the WGS 1984 Universal Transverse Mercator (UTM) 35S coordinate system, as the majority of available data falls within this UTM zone. UTM is a conformal projection, which utilizes a 2D Cartesian coordinate system to provide surface data positions. The UTM system is not a single map projection, but rather a series of smaller systems that subdivide the Earth's surface into sixty zones, each representing a 6° band of longitude, utilizing a secant Transverse Mercator projection in each zone.

4.2 Data Incorporation

Downhole drillhole logs are the primary subsurface dataset for informing the geometry of the modelled UG2 and Merensky Reefs away from surface traces or outcrops. The South African Council for Geosciences (CGS) has accumulated a substantial database of industry and governmental drillhole data over the BC. Available drillholes in the CGS database were identified, filtered and formally requested by the author. Scanned hard-copy logs were received from the CGS, however incorporation of these drillholes and their downhole data into the model proved challenging, as the majority of drillhole collar positions where either in unrecognised coordinate systems or did not contain any direct spatial information. However drillhole logs or layouts did incorporate surface plans that utilised local farm/municipal boundaries as references. As such, each plan was georeferenced using contemporary farm boundaries sourced from various municipal demarcation boards, with drillhole collar positions being subsequently extracted from these and projected into the UTM WDS 1984 35S system.

The depths of the logged UG2 and Merensky Reefs were then manually extracted from these logs and manually inserted into the Leapfrog drillhole database. Additional drillhole data was captured from publicly-available technical reports and incorporated prior to modelling. The final drillhole dataset comprises 380 historical drillholes, clustering on the Eastern and Western Limbs (Figure 4).

Regional, 1:250 000-scale maps were sourced from the CGS (2328 Pietersberg; 2330 Tzaneen; 2526 Rustenburg; 2528 Pretoria; 2530 Barberton; 2626 Wes-Rand; 2628 East Rand; 2426 Thabazimbi; 2428 Nylstroom; 2430 Pilgrims Rest; Walraven, 1989). These maps, which form the basis for numerous studies completed over the region, were incorporated (*viz*., georeferenced) into the geological modelling environment. Additional regional maps, published by Hunter (1975, 1976) and Hunter and Hamilton (1978), were also incorporated. A commercially-available map by Molyneux (2008), in collaboration with M. Frei, encapsulates the work of

Molyneux (1974), Molyneux and Klinkert (1978) with further observations derived from the archives at the Department of Geology, University of Pretoria. This map, which essentially covers a portion of the Eastern Limb, was purchased from the University of Pretoria and used as a referential backdrop. Where applicable, interpretations and structural observations on this map were incorporated into the modelling environment, although there are fewer interpreted structures on the Molyneux (2008) map.

A significant number of data, predominantly geochemical and mineralogical, are available in open-source or public domain technical person's reports (such as SAMREC Code or 43-101 compliant formats) issued by exploration and mining companies. Figures available from literature and technical reports tend to concentrate on relatively small and economically-viable areas or existing mines, predominantly in the Eastern, Western and Northern Limbs (Figure 4), and consequently these have received duly more attention than other areas (e.g. Southern Limb, Northern Limb, central portion of the Rustenburg Layered Series). Reef traces, field mapping, regional/local geophysical surveys and demarcated or inferred reef depths were digitized from these technical reports, draped onto high resolution topographic DEM surfaces to establish more accurate spatial attributes at surface, and incorporated into the modelling workflow. Where present, or interpreted from drillhole data in technical reports, the positions of UG2 and Merensky Reef contours, shown as either depth below average ground surface or elevations above sea level, were extracted from georeferenced figures. The resultant geospatial database comprises information derived from over 250 georeferenced maps and figures that have been captured and digitized (the majority of this database was received in georeferenced format). Reef positions (UG2, Merensky, LG and MG chromitites, magnetite reefs) from the aforementioned geospatial database (initially compiled by Basson 2019) were integrated into the 3D modelling environment, although emphasis was obviously placed on the UG2 and Merensky Reefs.

4.2.1 Geophysical Data Inversion

In order to guide the RBF at depth and in the centre of the Rustenburg Layered Series, other data sets need to be relied upon. In other words, the drilling made available by the CGS and extracted from competent persons reports is focussed on the Eastern and Western Limbs (and an aliquot of data on the Northern Limb, although this falls outside of the VOI), with no drilling data in the middle of the Rustenburg Layered Series. Contours, representing inferred depth of BC, generated from an unconstrained geophysical data inversion were used to guide the position and geometries of the modelled surfaces at depth. Such a combination of "hard" drillhole

data, with “softer” modelled data, in this case modelled in GoCAD, is a particular strength of Leapfrog and other implicit modelling packages.

The deep geometry of layered mafic intrusions has been inferred from density and gravity modelling on numerous occasions (Gupta and Sutcliffe, 1990; Deemer and Hurich, 1997; Armit *et al.*, 2010; Karinen, 2010; Williams *et al.*, 2016; Rezaie *et al.*, 2017), with several studies specifically addressing the BC (Eriksson and Reczko, 1995; Coomber, 2008; Cole *et al.,* 2014). Given the significant density contrasts between the mafic rocks of the Bushveld Complex and the surrounding granites and sediments, as well as contrasts across the crust–mantle boundary, gravity modelling sis viewed as an ideal tool for constraining the deeper portions of the 3D geometry of the BC (Cole *et al.*, 2014).

Geophysically-constraining or modelling of geological features relies on observable physical contrasts between geological entities. The recorded density/specific gravity of the various lithological groups hosting - and near- the RLS, as well as any intrusions or their layers, are detailed in Table 2. Furthermore, in the case of gravity modelling, a background value needs to be established so that a contrast can be determined and modelled. Cole *et al*'s (2014) constrained, 3D gravity modelling indicates the presence of contrasting dense within the area between the Eastern and Western Limbs, to significant depths. Conceptually, the simplest geometry to achieve similar density contrasts is to model the RLS as a single connected intrusion at depth. The incorporation of crustal thickness data, in conjunction with the gravity modelling, supports the concept of an interconnected BC model (Cawthorn and Walraven, 1998; Cawthorn and Webb, 2001; Webb *et al.*, 2004; Cole, *et al.*, 2014). Basson (2019) proposes that the Bushveld initially intruded as a largely symmetrical, predominantly flat lying body with equant N-S and E-W dimensions (an estimated 320 km by 320 km), further stating that it is likely that the BC exhibited a greater N-S/NNE-SSW extent than previously anticipated, prior to N-S oriented compression. These and other observations essentially provide conceptual starting models for data inversion

Table 2: Summarised densities of various lithological groups hosting and in close proximity to the Rustenburg layered Suite, derived from works completed by Ashwal et al., *(2005a, b),* Davis et al., *(2007), Coomber, (2008); Cole et al., (2014) and Jones, (2017).*

Summarised Densities of BC Host Units	
Upper Pretoria Group	2,720 kg/m^3
Rooiberg Granites	2,630 kg/m^3

Summarised Densities of BC Host Units	
Transvaal Supergroup	2,620 kg/m^3
Lebowa and Rashoop Granite Suites	2,630 kg/m^3
Undifferentiated granitic units	2,660±60 kg/m^3
Marginal Zone:	3,054 kg/m^3
Lower Zone	3,196 kg/m^3
Critical Zone	3,090 kg/m^3
Main Zone	2,920 kg/m^3
Upper Zone	3,110 kg/m^3
Ion-rich ultramafic pegmatoids	3,091 kg/m^3
Magnetic Susceptibly of Typical Mafic Units	
Dunite	0.125 SI units
Gabbro	0.09 SI units
Komatiites, tholeiites	0.12 SI units
Norite	0.09 SI units
Pyroxenite/hornblendite	0.25 SI units
Transvaal Supergroup	0.034 - 0.092 SI units.

A “heterogeneous Bushveld Complex” series of density values, proposed by Coomber (2008), which ranges from 2 870 kg/m^3 to 2 980 kg/m^3, highlights density contrast between various host sedimentary units, components of the BC/RLS and granite(s) (Webb *et al.*, 2004; Cole *et al.*, 2014; Basson, 2019). Detailed regional geophysical maps indicate notable gravity highs associated with well-studied or mapped limbs of the complex (Cawthorn and Webb, 2001; Webb *et al.*, 2004; Cole *et al.,* 2013) and possibly also magma feeder zones (Viljoen, 1999).

The magnetic susceptibility of the Rustenburg Layered Suite and its various components have also been summarised by several authors (Hattingh, 1991; Ferré *et al.*, 1999; Letts *et al.*, 2005; Ferré *et al.*, 2014, Campbell, 2011). Hemant (2003) summarises a suite of typical rock types, packages, and magnetic susceptibilities, which are also detailed in Table 2. The MZ and UZ boundary is well contrasted using magnetic susceptibility data. MZ cumulates typically show magnetic susceptibilities <0.05 SI units, down to <0.02 SI units (Hemant, 2003) while 1 - 5 m granitic sills in the MZ show a response of up to 0.7 SI units. More variability in magnetic susceptibility is apparent above the MZ/UZ boundary, due to contrasting anorthositic layer values below 0.1 SI units and magnetitite layers up to 5 SI units.

My BC implicit geological model incorporates products derived from an unconstrained density and gravity forward inversion modelling in 3D, performed in GoCAD and described in Basson (2019). From the CGS, a 3 km line-spaced regional airborne magnetic and gravity dataset was used in potential-field inversion modelling (see

Ledwaba *et al.*, 2009; Basson, 2019). The gravity and density models were generated by a Geophysicist, Jude King of XPotential in 2015, using GoCad and inverted using Fullagar's VPmg in a two-step process: basement inversion, then heterogeneous density inversion, using a cell size of 2,000 m horizontal x 100 m vertical. The values output from the inversion process reflect percentage changes or gradients for gravity (or density contrasts versus established or picked background values). These isoshells of magnetic susceptibility or density differences were incorporated into the 3D modelling environment, in Leapfrog, as a series of polylines or contoured isoshells, and should be regarded only as guides – rather than hard data – for the RBF-generation of UG2 and Merensky Reef surfaces at depth, away from borehole-derived contacts or reef traces at surface. This allows for the incorporation of geophysically constrained data, extrapolated from "hard" drillhole data.

4.2.2 Data Resolution: Disparities Due to Scale

To reiterate previous sections, the BC implicit model must incorporate numerous, multi-scale datasets, ranging in scale from country-wide geophysical datasets, discreet mapping points, dips and strikes derived from CGS and other maps, to contacts extracted from drillhole logs. Variability in data scale, distribution and historical interpretations proved problematic to resolve, as "mis-matches" in spatial or technical detail can result in unrealistic geometries being constructed, particularly where dataset conflict. These mismatches or conflicts do not necessarily denote or imply inaccuracies within the underlying datasets, but rather ways these datasets affect the manner in which they inform model construction and, consequently, the downstream utility of – or confidence in - the product. A systematic approach to resolve these discrepancies in scale was developed, whereby variably scaled data was reviewed and manually weighted according to the following criteria:

1. Modelled surface proximity (to nearby data);
2. Scale of capture (regional, local, discreet);
3. Date of capture;

Default surface construction prioritized proximal data, which was weighted higher than distal data, with two exceptions; 1) higher-resolution data are weighted or prioritised higher than low resolution data, where two or more datasets – or data points - were conflicting or in close proximity to one another; and 2) contemporary or more recent data was given a higher weighting than older records, should these conflict. Advances in digital systems have greatly improved the accuracy of digitally-captured data and large, computationally-complex datasets, such as regional geophysics and LIDAR/SCAN-LINE data, are now widely-used in industry. Thus,

discrepancies in variably-scaled data were resolved by weighting them against all other available data, following which data were “meshed” and incorporated into the implicit model. Regional geophysical studies, their interpretations, inversions and other products proved challenging to incorporate into the 3D environment, due to their contrast in resolution with respect to more regional datasets, like across individual limbs of the BC.

A working example of this discrepancy in scale is evident from the available Advanced Spaceborne Thermal Emission and Reflection Radiometer (ASTER) Digital Elevation Model (DEM) surfaces. Many data components, such as drillhole collars, did not have an associated z/elevation component, which is an essential requirement when modelling in 3D. To assign these values, geospatial data had to be draped onto a high-resolution DEM surfaces, of which two were available.

The first option is the GDEM V2 high-resolution ASTER DEM surface, available from the NASA EARTHDATA initiative, which is a joint operation wherein georeferenced satellite data captured by the Ministry of Economy, Trade and Industry (METI) of Japan and the United States National Aeronautics and Space Administration (NASA) are released as the ASTER Global DEM Version 2 (GDEM V2, released October 17, 2011). The GDEM V2 is available in GeoTIFF format, which is a standard, public-domain metadata product that allows georeferencing information to be embedded within the TIFF file (Mahammad and Ramakrishnan, 2003). The GDEM V2 GeoTIFF was imported into QGIS and used to generate elevation contours, at a spacing of 10 m, which were subsequently imported into the Leapfrog modelling environment and used to construct a high-resolution 3D wireframe of the DEM. The resultant ASTER DEM wireframe therefore has an accuracy of 30 m, thus any data draped onto this surface has an approximate vertical accuracy of 30 m.

The second option is the Stellenbosch University Digital Elevation Model (SUDEM), commercially hosted by Geosmart. SUDEM is a 5 m resolution DEM and is currently the highest resolution dataset available for South Africa, with a vertical accuracy of 2 - 15 m. The trade-off in this situation is that georeferenced objects with elevations assigned from the higher resolution SUDEM are computationally more complex, as they record local, very minor variations in elevations, compared to that of the GDEM V2. It was resolved that drillhole collars, georeferenced reef/marker horizon contours and field mapping datapoints should derive their elevations from the SUDEM DEM, with the remaining datasets elevations derived from GDEM V2 DEM, in order to improve the iterative, computation time.

4.3 Fault Network Construction

The fault network (Figure 5) was modelled from digitized polylines and structural orientation data, with local elevation values generated from the SUDEM. As described previously, interactions (viz., the chronology) between each modelled fault were established. To re-iterate: these interactions comprise rules that define 3D cross-cutting or terminating relationships between each fault, by explicitly establishing a relative "surface chronology" within the 3D software. This fault chronology requires the establishment of relative fault terminations and ages. To determine this, a relative weight of evidence approach was adopted, whereby structures with the highest amount of supporting data were prioritised within the chronology.

Faults with the greatest supporting data, or that are acknowledged in the literature as major zones of displacement, were "activated" in the software. Activation of 13 faults renders them as hard modelling boundaries, which structurally sub-domain volumes (see Figure 5). Sub-domaining or compartmentalization allows for the local incorporation of block-specific modelling parameters on a volume-by-volume basis. For a fault to terminate against another fault, it must be lower in the fault chronology (i.e. older). Several lower-confidence faults were identified but, with little relevant supporting spatial data, are modelled but are not used to sub-domain the initial modelling volume.

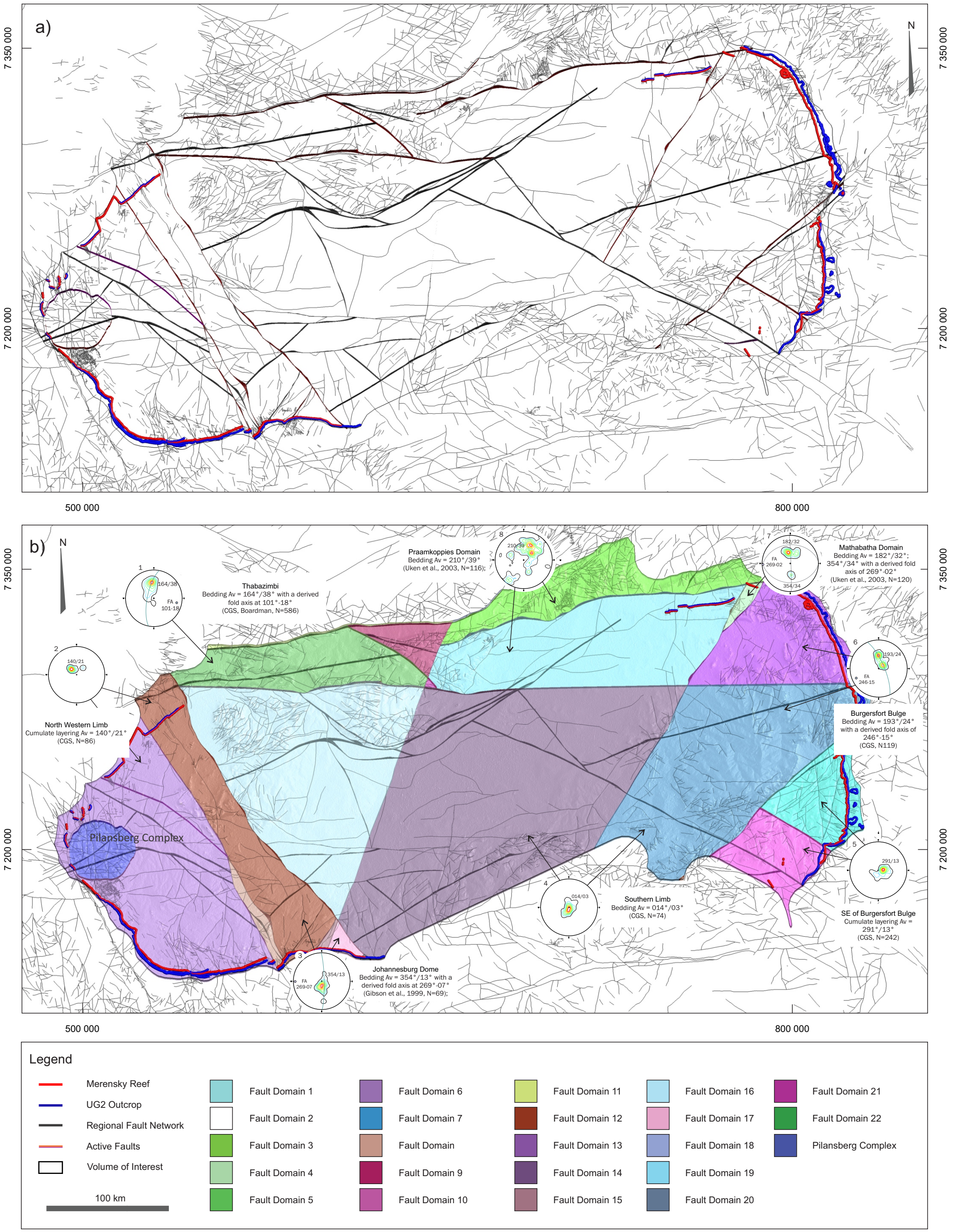

Figure 5: Modelled fault network. A total of 63 key regional structures were identified and modelled in 3D (a). Of these, 13 were activated within the software, to delineate fault domains (b). A total of 23 fault domains were constructed. Merensky and/or UG2 surfaces are not modelled in several fault domains due to the paucity or lack of outcrop or downhole data. Static structural trends were utilised for initial reference surface construction, which varied per fault domain. These structural trends were derived from stereonet analysis and contoured averages of cumulate layering measurements, if available, regional bedding orientations (stereonets are equal area, lower hemisphere). This data sourced from Basson (2019), as well as incorporating additional data acquried from more recent works.

4.4 Surface Construction Technique

Shortcomings in software capability necessitated that the methodology used to generate the key marker reefs be subdivided into three primary components (see modelling workflow detailed in Figure 6):

1) Construction of reference surfaces for both Merensky and UG2 reefs;
2) Construction of structural trends, incorporating geophysical and mapping data;
3) Construction of final surfaces.

4.4.1 Reference Surface Construction

Reference surfaces are required for the application of software-related tools and features on such a widely-distributed set of apparently disparate data. Foremost amongst these tools is the ability of the software to utilise non-contacting structural data to inform surface construction, using the Structural Trend (ST) tool. This tool creates a search ellipsoid anisotropy that varies in direction. Reference surfaces for the UG2 and Merensky Reefs were constructed, utilising contacts derived from drillhole logs and surface mapping. These reference surfaces utilised static guiding trends (fault domain-specific trends displayed in Figure 5), in turn derived from various technical reports and studies, to guide their construction. Given the extent of data distribution, the deposit surface tool (DS) was selected to construct the UG2 and Merensky reference surfaces, as it allows for construction of the most robust reference surfaces, requiring a minimum of explicit controls. The DS accomplishes this by explicitly intersecting specified contacts or intervals, even over vast distances. Surface construction is dictated by mapping and downhole contacts, orientation data and regional trends, constructed in accordance with their overall geometry rather than their genesis (Figure 3).

Control points were then derived from the modelled UG2 and Merensky Reef reference surfaces, which denote both the position and orientation of the related surface triangulation. Given the scale of the model, these control points required simplification or declustering prior to downstream use. Declustering is the procedure whereby large datasets are reviewed, sets of typical orientations delineated, and averages, per set calculated, over specified distances or volumes. Another software package, Micromine, was utilized to decluster the resultant reference surface control point files into more manageable files. Derived control points were declustered within a 1 km buffer zone, which provided a calculated mean point orientation, for all points within a 1 km radius. These control points were then reimported into the BC Leapfrog model space.

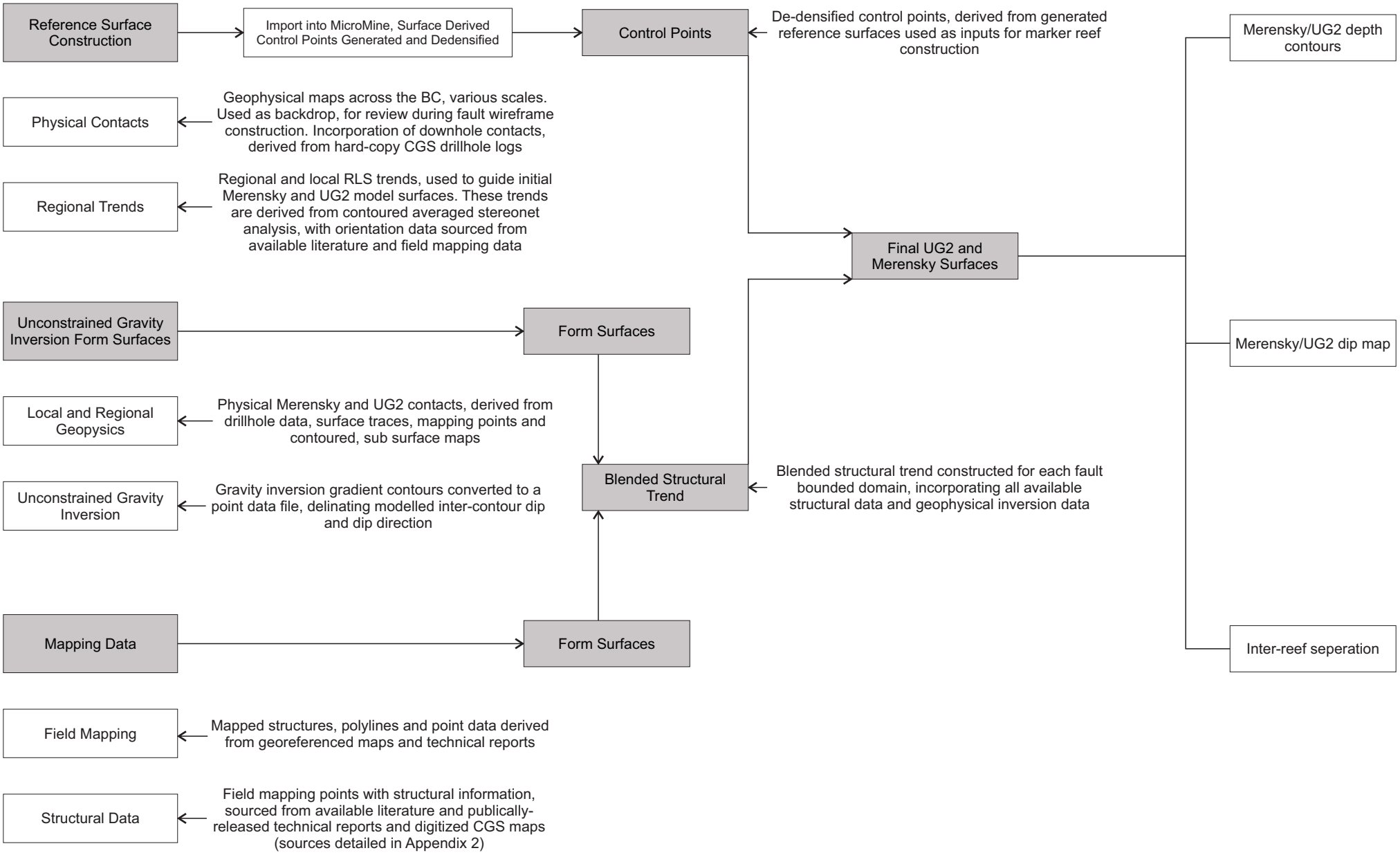

Figure 6: Schematic of modeling workflow used for the construction of the UG2 and Merensky Reef surfaces

4.4.2 Construction of Structural Trends

The Structural Trend tool generates a roaming ellipsoid ratio (effectively a flattened sphere representing an anisotropy) that varies in direction and strength according to an input triangulation, surface or structural measurement. These ellipsoid ratios determine local search trends, which in turn determine the local weighting of data informing surface construction. These structural trends may be viewed as a series of “flattened spheres” in 3D space, where the orientation of the sphere provides the direction of the anisotropy, while the size of a disk is proportional to the local anisotropic strength.

A structural trend was constructed per fault domain, to inform final surface construction trends within each of these domains. These structural trends were required to incorporate both disparate field mapping and geophysical inversion data.

4.4.3 Incorporation of Inversion Results

As indicated previously, contoured isoshells of gravity contrasts, representing the apparent depth of the RLS, were used as a guide for the RBF-generated UG2 and Merensky surfaces at depth and away from borehole-derived contacts or reef traces at surface. Incorporating the gravity inversion products required additional processing prior to incorporation into modelling procedures. Unconstrained gravity inversion contours were used to construct a series of reference surfaces, from which control points, indicating the spatial position and orientation of the resultant contours, may be drawn. These reference surfaces were constructed at a high modelling resolution (500 m inter-triangulation lengths), to ensure a robust control-point cloud. Multiple resultant surfaces were reviewed, to ensure that the most geologically representative surface was selected for modelling procedures.

Gravity highs are identified where the RLS becomes approaches the surface towards the West in the Western Limb and to the East in the Eastern Limb. Upon review of the control point file, it was noted that the control points indicate a down-dipping geometry just beyond RLS surface outcrop to West and East of their respective limbs. This apparent down-dipping geometry is due to the decrease in the density signal beyond the surface exposure of RLS, and these inappropriate or non-representative down-dipping control points were selectively removed.

To ensure that this dataset was effectively incorporated, two regional form interpolants, were generated. A form interpolant is a representative surface, or series of surfaces, that emulates broad trends in 3D. It may be used as inputs for structural trend generation. Separate form interpolants were generated, one derived from the unconstrained gravity inversion and the other from compiled field mapping data.

The resultant surfaces for these form interpolants were used as primary inputs for fault domain-specific structural trends, resulting in a “blended” structural trend that incorporates all available structural data. The resolution of the structural trend is determined by the size of the modelling block in question; in other words, this is a non-parametric value that currently cannot be adjusted within the software.

4.4.4 Application of Structural Trends

UG2 and Merensky contact surfaces were constructed, incorporating declustered control points and initial hard lithological contacts/surface traces, informed by fault domain-specific structural trends. These surfaces were constructed as intrusion contact surfaces, which allows for the implementation of the ST tool.

5 Modelling uncertainty or confidence

A basic geological principle is the development of three-dimensional models of subsurface rock, derived from the application of geological theories to a series of observations. A model is required as it is generally not feasible to precisely observe subsurface geology. Two or 3D modelling confidence, or inversely, modelling uncertainty, is primarily derived from two key components:

1. Uncertainty related to data, and
2. Uncertainty derived from interpretation.

There is a distinction between uncertainty connected with the quantity of data, versus the uncertainty associated with the quality of interpretation. The methodology used to determine the uncertainty in the BC model will primarily address data uncertainty, which in turn directly impacts modelled features. Assessment of geological confidence, or the likelihood that modelling results fully represent reality, is difficult to quantify as this uncertainty is dependent on several factors (Funtowicz and Ravetz, 1990). These factors include the following key elements:

- Data quality;
- Data collection methodology and calibration;
- Calibration;
- Objectivity;
- Interpreters experience.

Quantifying geological confidence would require the assessment of each of these key elements, with the development of a relative confidence score determined by an arbitrary attribution of a relative score to best describe the confidence, or “truthfulness” of each element. This score would be numerically averaged to determine an overall quality score (Funtowicz and Ravetz, 1990). The disparate nature in the distribution, source, age of input datasets and lack of access to original authors of data capture or interpretations has resulted in an absence of meta-data for input datasets, which has the added effect of making the aforementioned confidence assessment impractical or unrepresentative.

Firstly, the quantity and distribution of data in a given volume for interpretation is fundamental to the reliability or confidence in the final interpretation. For the BC model confidence assessment, the distribution of data was evaluated for the VOI. The reasons for this are twofold – implicit/mathematical modelling will always return the same results if the same conditions are applied to the same underlying database, rendering traditional modelling sensitivity analysis somewhat moot, with the *distribution* and *relative concentration* of input data having a higher effect on resultant surface/volume construction than the *type* of data.

Secondly, this represents the most practical way to generate a coherent overview of modelling confidence, using a set spatial grid to assess the density and distribution of data. Two separate maps were generated, one for "hard data" such as drillhole intersections and surface reefs (Figure 7a), and the other for inferred, derived or "soft data" such as geophysical inversion contours (Figure 7b). These maps are representations of the relative distance from, and influence of, these general data types.

Distance to data is used as a proxy for relative modelling confidence, with Figure 7 – not surprisingly - indicating a direct or linear trend in confidence as distance from underlying data increases. Results within the buffer region of 1 – 2 km are considered "high" confidence with regards to their results. High confidence is taken to be a quantity (or a quantity) of data that is considered optimal for interpretation. This approach has implications associated with both practicality and retrospectivity of the geological data, with regards to both model scale and intended use, which ties in further into what is defined as an ideal amount of data. Given model construction techniques, model use, geological aspects and interpretation, it should be noted that ideal data density and distribution is that when further incorporation of data has no discernible effect on modelling results. Thus, what is defined as ideal data is differs, and should be reviewed on a case by case basis. The remaining confidence scores (moderate, low and very low) form linearly distributed categories that range from ideal data density scenarios to where data is zero.

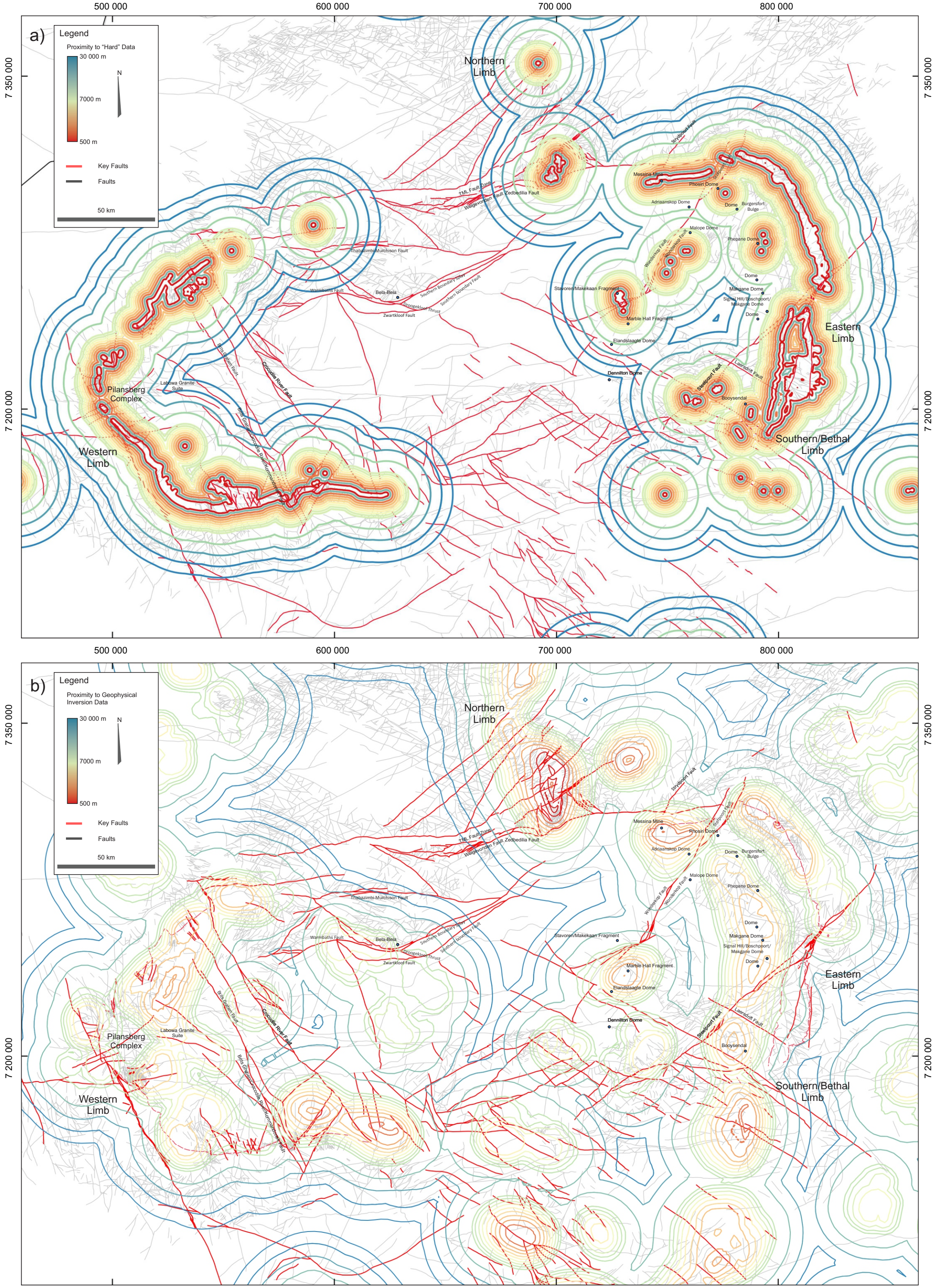

Figure 7: a) Contours indicating distance to "hard" input data, such as drillhole contacts, surface reef outcrop and subsurface reef contours. b) Contour map indicating proximity to geophysical inversion data. Whilst not used as a direct control, geophysical inversion contours provided a reference trend for modelled surface delineation.

6 Results

The modelled Merensky Reef, UG2 Reef and form interpolant surfaces are displayed in Figure 8. Subsidiary modelling outputs derived from the aforementioned contact surfaces were also generated. These include contoured depth, surface dip and inter-reef separation. Reef depth maps for the Merensky (Figures 9) and UG2 Reefs (Figure 10) were contoured at a vertical inter-contour spacing of 10 m. Western Limb Merensky and UG2 Reef depth contours indicate substantial increases in depth (- 3000 m MASL) towards the centre of the complex, east of the Crocodile River Fault, although one needs to take into consideration the effects of extrapolation into areas with few actual data constraints, where the surface construction defers to regional geophysical data. This increase in depth is coincidental with areas overlain by the Lebowa Granite Suite (positions indicated on Figures 9 - 11). The modelled Merensky and UG2 modelled reefs shallow to the east of the Crocodile River Fault, indicating a trough-like depression to the west (e.g., accommodated by vertical displacement along the crocodile River Fault). The Merensky Reef also shows significant variations in depth across the Brits Graben Fault, although this structure appears to have affected the depth and/or depth variation of modelled UG2, in this area, only to a lesser extent.

Moving eastwards, the UG2 and Merensky Reefs again show an increase in depth (- 1700 m MASL) towards the Waterberg Basin, north of Bela-Bela, in an area dominated by faults and thrusts of the TML and the Zwartloof Fault, although this increase in depth is more apparent in modelled UG2 reef contours. Modelled reefs shallow significantly towards the Marble Hall Fragment, Dennilton Dome and the Steelpoort Fault. Modelled Merensky and UG2 Reefs appear to be locally disrupted by minor domes within the Eastern Limb (e.g. Signal Hill/Boschpoort/Makgane Domes), although their depth appears to be relatively consistent east and northeast of the Burgersfort Bulge. Reefs shallow significantly to the SE of the Steelpoort Fault, north of Booysendal Mine.

Modelled inter-reef separation was calculated and is presented in Figure 11. Zones of anomalously large inter-reef separation were identified and labelled 1-12. Upon review, it was established that several anomalous inter-reef separation areas (areas denoted 1 - 6) appear to be modelling artefacts, caused by disparities in data availability for the modelled Merensky Reef and the effects of (over-)extrapolation. One of these effects or artefacts is an artificially-raised Merensky reef surface, due to the modelling interpolant attempting to connect data that are typically positioned at a greater average height than what is appropriate for given fault-domains. across the modelling VOI.

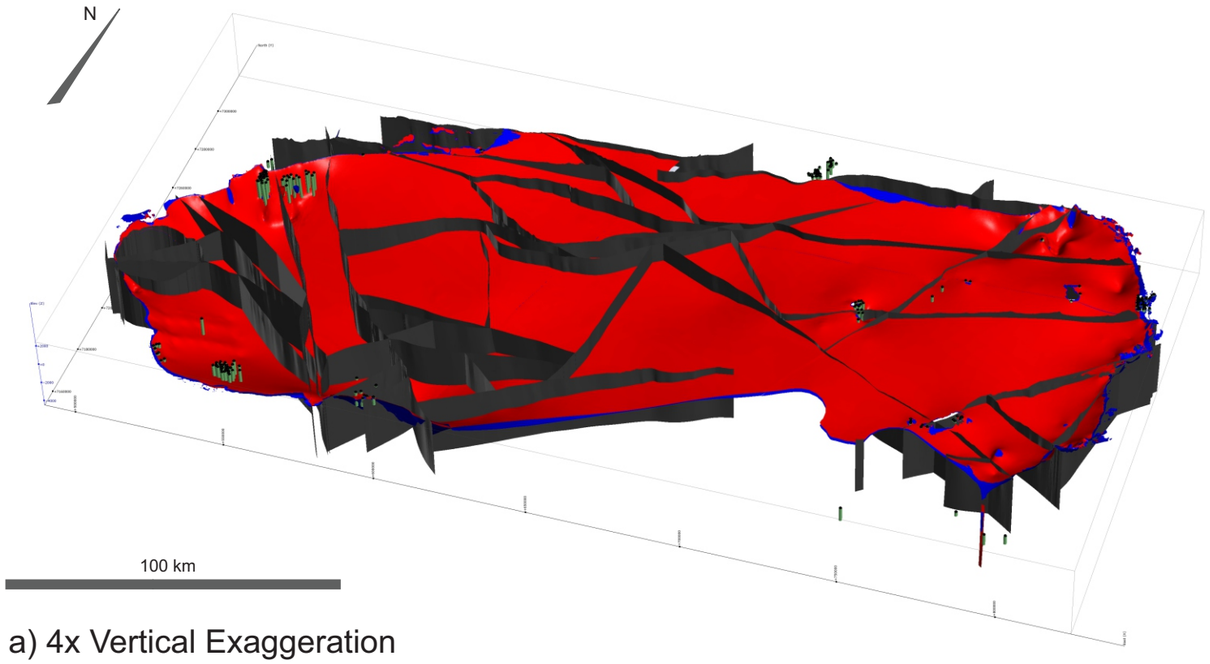

a) 4x Vertical Exaggeration

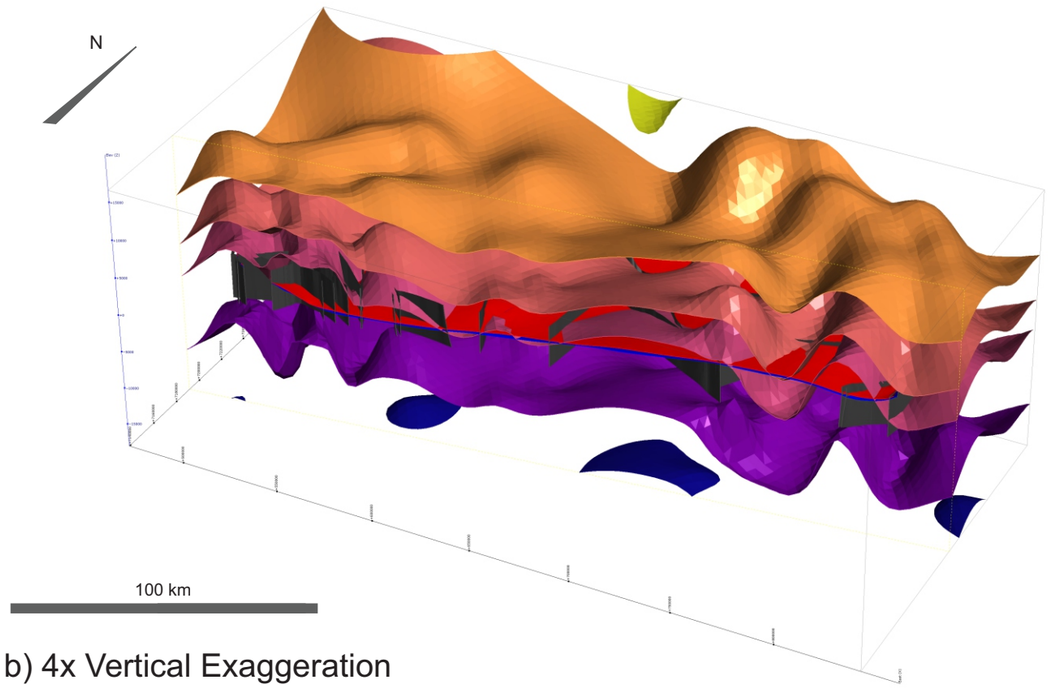

b) 4x Vertical Exaggeration

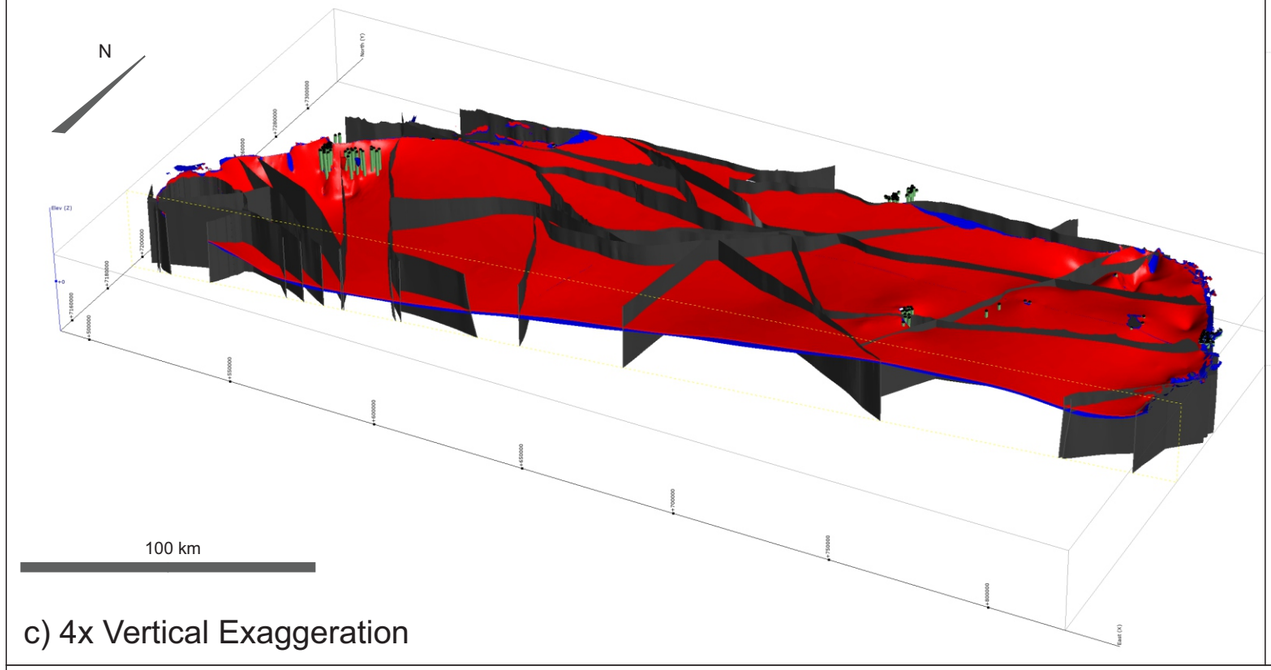

c) 4x Vertical Exaggeration

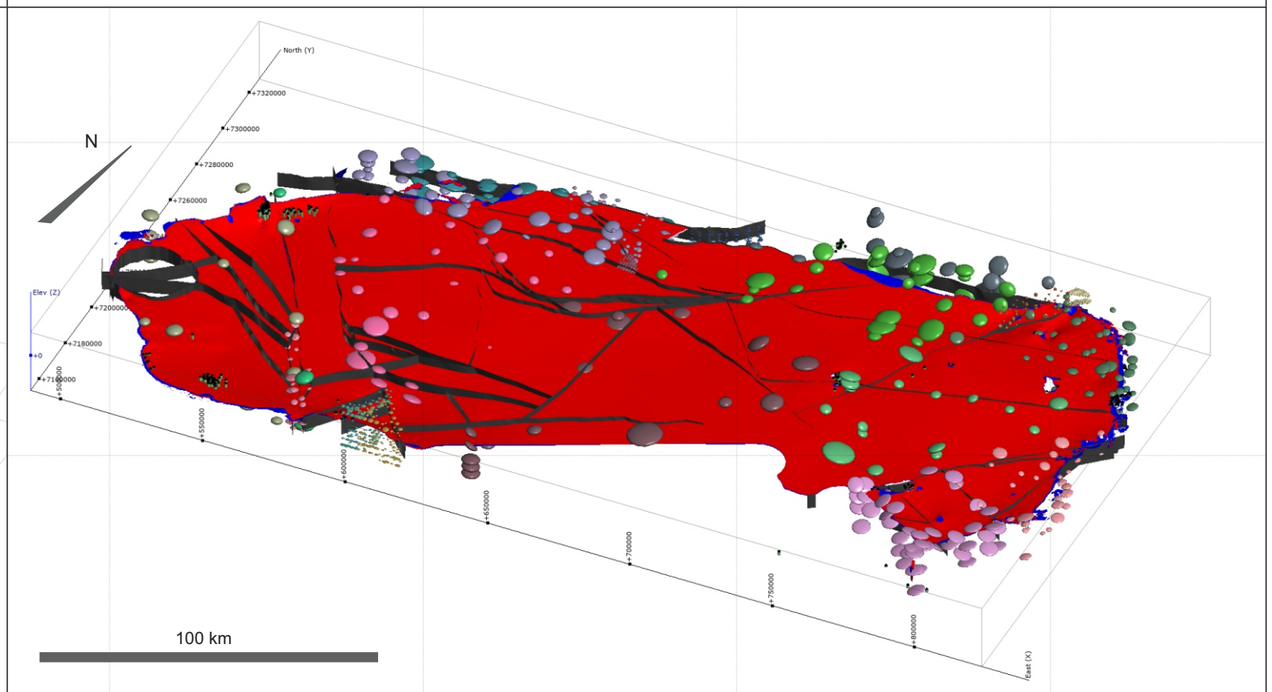

d) 1x Vertical Exaggeration

Legend

- Drillhole Collars
- Structural Trend Position and Orientation
- Merensky Surface
- UG2 Surface
- Modelled Faults
- Drillhole Traces
- Unconstrained gravity Form Interpolants

Figure 8: Modelled Merensky and UG2 reef surfaces. Distribution of drillhole data and modelled fault network; b) Form interpolant surfaces, derived from unconstrained gravity inversion; c) E-W section drawn through BC; d) Distribution and strength of structural trends constructed per modelling block.

500 000 600 000 700 000 800 000

7 350 000

7 200 000

Legend

- Drillhole Collars
- Merensky Reef
- UG2 Outcrop
- MG Chromitites
- LG Chromitites
- Magnetite Reefs
- Other Reef Outcrop
- Digitized Reef Contours
- Key Faults
- Key Dykes
- Faults
- Gravity Inversion Contours
- Volume of Interest
- Labowa Granite Suite
- Ultramafic Pegmatoids

Elevation (MASL)

1950 m

-1700 m

-3500 m

N

100 km

Northern Limb

Eastern Limb

Western Limb

Southern/Bethal Limb

Pilansberg Complex

Labowa Granite Suite

Messina Mine

Phosiri Dome

Adriaanskop Dome

Dome

Burgersfort Bulge

Malope Dome

Phepane Dome

Dome

Makgane Dome

Signal Hill/Boschpoort/ Makgane Dome

Dome

Stavoren/Makekaan Fragment

Marble Hall Fragment

Elandslaagte Dome

Dennilton Dome

Booysendal

Bela-Bela

Zwartkloof Fault

Warmbaths Fault

Thabazimbi-Murchison Fault

TML Fault Zone

Welgevonden Fault

Zedbedilia Fault

Strydpoort Fault

Strydpoort Fault

Wonderkop Fault

Wonderkop Fault

Southern Boundary Splay

Southern boundary Fault

Droogekloof Thrust

Brits Graben Fault

Crocodile River Fault

Brits Graben/Crocodile River/Kommanonder Fault

Steelpoort Fault

Laersdrift Fault

Figure 9: Merensky elevation contours (MASL)

500 000 600 000 700 000 800 000

7 350 000

7 200 000

Legend

- Drillhole Collars
- Merensky Reef
- UG2 Outcrop
- MG Chromitites
- LG Chromitites
- Magnetite Reefs
- Other Reef Outcrop
- Digitized Reef Contours
- Key Faults
- Key Dykes
- Faults
- Gravity Inversion Contours
- Volume of Interest
- Labowa Granite Suite
- Ultramafic Pegmatoids

Elevation (MASL)

1950 m

-1700 m

-3500 m

N

100 km

Northern Limb

Eastern Limb

Western Limb

Southern/Bethal Limb

Pilansberg Complex

Labowa Granite Suite

TML Fault Zone

Welgevonden Fault

Zedbedilia Fault

Thabazimbi-Murchison Fault

Southern Boundary Splay

Southern boundary Fault

Droogekloof Thrust

Zwartkloof Fault

Bela-Bela

Brits Graben Fault

Crocodile River Fault

Brits Graben/Crocodile River/Commando Fault

Strydpoort Fault

Messina Mine

Phosiri Dome

Adriaanskop Dome

Dome

Burgersfort Bulge

Malope Dome

Phepane Dome

Wonderkop Fault

Stavoren/Makekaan Fragment

Dome

Makgane Dome

Signal Hill/Boschpoort/ Makgane Dome

Dome

Marble Hall Fragment

Elandslaagte Dome

Dennilton Dome

Steelpoort Fault

Laersdrift Fault

Booysendal

Figure 10: UG2 elevation contours (MASL)

Modelled inter-reef separation is fairly consistent along the majority of the Western Limb, particularly in proximity to reef outcrop, with a typical separation from 10 m to 50 m. The northern part of this limb is kown to host many potholes - these local features in inter-reef separation are averaged out and/or so minor that these features do not fall within the model resolution. This pattern is locally disrupted east of the Elandsdrift Fault, towards the Krokodildrift Section, where inter-reef separation rapidly increases, and in some cases is in excess of 400 m (Point 7). Separation apparently increases around the boundaries of the Pilansberg Complex, ranging between 100 m and 200 m (Point 8). High modelled inter-reef separations (400 m to 500 m) are apparent between the Middellaagte Graben Bounding Fault and the northern portion of the Crocodile River Fault (Point 9). This separation decreases southwards, towards the centre of the western portion of the Lebowa Granite Suite. West of the Dennilton Dome (Point 10), to the south of a regional dyke, modelled reef separation increases to 300 m and even up to 350 m. Similar to the Western Limb, the modelled Eastern Limb Merensky and UG2 Reef separation is largely consistent in proximity to reef outcrop, with separation distances constrained to between 10 m and 100 m. Reef separation increases dramatically to the northeast of the Dwarsrivier Splay, in close proximity to Kennedy's Vale Mine (Point 11), with modelled inter-reef separation ranging from 300 m to 500 m. Similarly, anomalously high modelled reef separation is again evident south of the Laersdrift Fault (Point 12). Moderate inter-reef spacing is apparent in the vicinity of the Marble Hall Fragment (100 m to 200 m), increasing dramatically towards the SE, although high inter-reef spacing appears to dissipate or is inconsistent near several regional dykes (Point 13).

Modelling artefacts, particularly those relating to modelled depths, are to be anticipated in a geological model of this scale and complexity, using widely separated and locally disparate data sets. As the implicit modelling function attempts to generate a best fit curve through control points and other hard data, areas of sparse data are likely to produce resultant surfaces that over-simplify surfaces or be unrepresentative of geological features where the tectonostratigraphy changes abruptly. Furthermore, implicitly modelled surfaces and resultant solids may extrapolate unrealistically outwards and away from constraining data towards model boundaries. These instances have to be noted and mitigated, where possible. Notwithstanding this, it is apparent that implicit 3D geomodelling over such a large area is eminently possible, however, modelling assumptions need to be carefully established.

500 000 600 000 700 000 800 000

7 350 000

7 200 000

Legend

Drillhole Collars
Merensky Reef
UG2 Outcrop
MG Chromitites
LG Chromitites
Magnetite Reefs
Other Reef Outcrop
Digitized Reef Contours

Key Faults
Key Dykes
Faults
Gravity Inversion Contours
Volume of Interest
Labowa Granite Suite
Ultramafic Pegmatoids

Seperation
< 20 m
200 m
500 m

N

100 km

Northern Limb

Eastern Limb

Western Limb

Southern/Bethal Limb

Pilansberg Complex

Labowa Granite Suite

Messina Mine
Phosiri Dome
Adriaanskop Dome
Dome
Burgersfort Bulge
Malope Dome
Phepane Dome
Dome
Makgane Dome
Signal Hill/Boschpoort/ Makgane Dome
Dome
Kennedy's Vale mine
Stavoren/Makekaan Fragment
Marble Hall Fragment
Elandslaagte Dome
Dennilton Dome
Booysendal

Strydpoort Fault
Olifantspoortfault
TML Fault Zone
Weltevreden Fault
Zedbedilia Fault
Thabazimbi-Murchison Fault
Southern Boundary Splay
Southern Boundary Fault
Droogekloof Thrust
Zwartkloof Fault
Wonderkop Fault
Wonderkop Fault Zone
Dwarsriver Splay
Steelpoort Fault
Laersdrift Fault
Middellaagte Graben Bounding Fault
Brits Graben Fault
Crocodile River Fault
Brits Graben/Crocodile River/Kommandonek Fault
Hlanolsdrift Fault

1 2 3 4 5 6 7 8 9 10 11 12 13

Krokodildrift Section

Figure 11: Calculated inter-reef separation (m)

Dip maps, indicating the general dip range of the Merensky and UG2 Reefs, are displayed in Figures 11 and 12. Dips steepen towards surface reef outcrops across both the Western and Eastern Limbs of the BC. Anomalously steeply-dipping modelled Merensky and UG2 Reef are observable towards the northern and southern terminations of the Western Limb (see cross-section on Figure 12). The extent of these steep dips possibly extends eastwards from the Crocodile River Fault system, for approximately 5 000 km to 6 000 km (Point 1). Extensive and pervasive steepening of the modelled Merensky and UG2 Reefs is observed to the north of the Welgevonden Fault Zone, although this steep dip is more relatively pervasive or apparent in the contoured UG2 Reef dip map (Point 2). Anomalously steep dips are observed to the north of the Wonderkop Fault splay and extend southwards towards the Stavoren/Makekaan Fragment (Point 3). Large zones of almost horizontal reef are noted towards the apparent or inferred centre of the Rustenburg Layered Series (Point 4), and towards the southern portion of the Eastern Limb (Point 5), forming broadly concentric “domes” of low average dips. A general steepening of the modelled UG2 Reef surface and cumulate layering dip (< 50°) (stereonets in Figure 5) is observed towards the Zebedelia Fault and the northern edge of the Eastern Limb (Point 6).

500 000 600 000 700 000 800 000

7 350 000

7 200 000

Legend

Drillhole Collars
Merensky Reef
UG2 Outcrop
MG Chromitites
LG Chromitites
Magnetite Reefs
Other Reef Outcrop
Digitized Reef Contours

Key Faults
Key Dykes
Faults
Gravity Inversion Contours
Volume of Interest
Labowa Granite Suite
Ultramafic Pegmatoids

Modelled Reef Dip
0° 0.5° 1° 2° 3° 4° 5° 10° 20° 50°

N

100 km

Northern Limb

Eastern Limb

Western Limb

Southern/Bethal Limb

Pilansberg Complex

A A’

1 2 3 4 5 6

TML Fault Zone
Welgevonden Fault
Zedbedilia Fault
Strydpoort Fault
Thabazimbi-Murchison Fault
Southern Boundary Shear
Southern boundary Fault
Droogekloof Thrust
Zwartkloof Fault
Bela-Bela
Rustenburg Fault
Crocodile River Fault
Brits Graben/Crocodile River/Kommandonek Fault
Wonderkop Fault
Steelpoort Fault
Laersdrift Fault

Messina Mine
Phosiri Dome
Adriaanskop Dome
Dome
Burgersfort Bulge
Malope Dome
Phepane Dome
Dome
Makgane Dome
Signal Hill/Boschpoort/ Makgane Dome
Dome
Stavoren/Makekaan Fragment
Marble Hall Fragment
Elandslaagte Dome
Dennilton Dome
Booysendal

A A’

5x Vertical exaggeration

Figure 12: Modelled Merensky surface dips. Position of section line A-A’ indicated on map

500 000 600 000 700 000 800 000

7 350 000

7 200 000

Legend

Drillhole Collars
Merensky Reef
UG2 Outcrop
MG Chromitites
LG Chromitites
Magnetite Reefs
Other Reef Outcrop
Digitized Reef Contours

Key Faults
Key Dykes
Faults
Gravity Inversion Contours
Volume of Interest
Labowa Granite Suite
Ultramafic Pegmatoids

Modelled Reef Dip
0° 0.5° 1° 2° 3° 4° 5° 10° 20° 50°

N

100 km

Northern Limb

Eastern Limb

Western Limb

Pilansberg Complex

B

B’

Southern/Bethal Limb

TML Fault Zone
Welgevonden Fault
Zedbedilia Fault
Thabazimbi-Murchison Fault
Southern Boundary Splay
Southern boundary Fault
Droogekloof Thrust
Zwartkloof Fault
Brits Graben Fault
Crocodile River Fault
Brits Graben/Crocodile River/Kommandonek Fault
Strydpoort Fault
Wonderkop Fault
Steelpoort Fault
Laersdrift Fault

Messina Mine
Phosiri Dome
Adriaanskop Dome
Dome
Burgersfort Bulge
Malope Dome
Phepane Dome
Dome
Makgane Dome
Signal Hill/Boschpoort/ Makgane Dome
Dome
Stavoren/Makekaan Fragment
Marble Hall Fragment
Elandslaagte Dome
Dennilton Dome
Booysendal

1 2 3 4 5 6

B B’

5x Vertical exaggeration

Figure 13: Modelled UG2 surface dips. Position of section line B-B’ indicated on map

7 Discussion

The construction of a 3D, implicitly-modelled geological model, involving the generation of representative Merensky and UG2 Reef surfaces across the Rustenburg Layered Series of the Bushveld Complex, using open-source and public-domain data, has been demonstrated. Multiple data sources, modelling workflows and solutions were explored, in an attempt to account for the disparities in data resolution, data spacing/clustering, model scale and output generation. Resultant geometries and interpretations are, however, dependent on data distribution and quality, which is the case in any 3D model. However, the position and incorporation of additional data will have a significant impact on modelling results and such data, be it geophysical or direct, are likely to be more impactful towards the centre of the geological model where, in this case, available data are currently almost non-existent. A series of 2D seismic sections, which may have already been obtained by mining and exploration companies, would be particularly helpful in refining the 3D model, which, together with the workflow, was constructed with the intent of iteratively incorporating additional data, and further activation of existing or additional faults.

This, in conjunction with more local- or mine-scale comparisons, would provide robust outputs that should be more amenable to interpretation, as the local, higher-resolution data will have a greater impact on model results within smaller fault domains, wherein information is “diluted”.

7.1 Establishing the Confidence or Uncertainty in the Geological Interpretation

Data density and distribution are used as a proxy for modelling confidence (Figure 7). Given the multitude of sources of uncertainty in geological modelling (in both 2D and 3D studies), uncertainty related to issues other than data distribution and density was not addressed. An objective, consistent and methodical approach to evaluating geological confidence, with regards to both modelling and geological uncertainty, is yet to be fully implemented in the geological sciences, although a proxy for inferred uncertainty may simply be distance to model input data.

Resultant data density distribution plots indicate a lack of confidence towards the central and south eastern margins of the BC. It is the authors suggestion that this lack of confidence or underlying data may be addressed in future studies and model updates, by incorporating regional seismic studies or additional geophysical data, should these become available.

7.2 Modelled Features and Trends Related to Deformation

The northern portion of the Eastern Limb appears to be absent to the west of Messina Mine. The Merensky and UG2 Reefs shallow, and then steepen north-upwards, towards and along the TML, Zebediela and/or Welgevonden/Southern Fault systems. Additionally, the Eastern Limb becomes progressively more faulted, evidenced by rapid shallowing of both reefs (Figures 6, 8), towards the northern margin and in proximity to the left-lateral Stofpoort/Wonderkop Fault system. This apparent uplift and steepness along the northern model margin, in conjunction with the development of the Stofpoort/Wonderkop Fault System(s), likely developed in response to initial N-S compression of the complex (Good and De Wit, 1997; Basson, 2019). This southward vergence is also evident from the Droogekloof Thrust - Southern Boundary Fault system near the Thabazimbi/Rooiberg area (Basson, 2019).

Elevation plots indicate deep, relatively undeformed Merensky and UG2 Reef geometries east of the Crocodile River Fault, with Merensky and UG2 Reefs apparently shallowing eastwards. Notwithstanding this, the Rustenburg Layered Series to the west of the Crocodile River Fault appears to have experienced N-S flattening, if one proposes an initially more rounded, flatter-dipping magma chamber in plan view. Anomalous inter-reef separation, significant depths and steep bedding angles at the northern and southern terminations of the Western Limb likely indicate that southward vergence due to N-S compression is more clearly or unambiguously evident in the southern portions of the Western Limb, in proximity to the termination of the Krokodildrift Section. This is further evidenced by the presence of low-angle bedding or cumulate-layer parallel shears recorded in underground platinum mines (Clarke *et al.*, 2000; Basson, 2019). These observations, in conjunction with the homogenous reef dip in the area, indicate that the Crocodile River Fault has likely acted as a regional strain barrier, effectively partitioning strain between the Western Limb (flattened, but not rotate) and the remaining 2/3^{rds} of the Rustenburg Layered Series. As a result, the Western Limb also appears to be deeper, i.e. WL has been relatively down-faulted along the Crocodile River Fault, yet is still exposed at surface.

Another pattern emerges from the inter-reef separation map: there is a zone of apparently low inter-reef separation, approximately 50 km SW of the Dennilton Dome. Deformed Transvaal Supergroup inliers occur in the BC, the most prominent of which are the Crocodile River Dome (western Transvaal Basin), the Dennilton-Marble Hall Dome and Stavoren Fragment (eastern Transvaal basin), which consist predominantly of deformed lower Transvaal units that underwent low grade metamorphism (Hartzer, 1995). Positions and distributions of

low dip angles, in conjunction with the positions of various domes towards and in the Eastern Limb, may suggest a forward propagating thrust system that could have transported fragment (= domes) southwards to the east of the Crocodile River Fault.

In the area between the southern terminations of the Eastern and Western limbs, moderate reef depths, low inter-reef separations and moderate reef dips emerge from the 3D modelling, suggesting that reefs in this area are likely to have been only moderately deformed during southerly vergence or have been transposed into parallelism with thrusts. Basson (2019) proposed that the offset between the Southern Limb and the southern termination or tip of the Western Limb was right-lateral, accommodating an apparent 35° rotation anticlockwise of the volume to the east of the Crocodile River Fault, with the initial BC body behaving in a ductile manner at depth, while strain accommodation near-surface was brittle or brittle-ductile, in a collection of mutually cross-cutting "relay faults". The coincidence of deep reef and the overlying presence of the Lebowa Granite Suite has been observed; however, a direct spatial relationship between reef depth and overlying granites has not yet directly addressed or noted in the literature.

8 Conclusions

This thesis details the construction of a 3D, implicitly-modelled, proof-of-concept geological model, involving the generation of representative Merensky and UG2 Reef surfaces across the Rustenburg Layered Series of the Bushveld Complex, using open-source and public-domain data at a variety of scales and in a variety of initial co-ordinate systems. Multiple data sources, modelling workflows and solutions were explored, in an attempt to account for the disparities in data resolution, data spacing/clustering, model scale and output generation. Merensky and UG2 Reef elevations, surface dips and calculated inter-reef separation were subsequently interrogated in light of known or mapped features (e.g. faults, domes, extents of limbs).

Geological anomalies, trends or features were identified, such as the regional steepening of modelled Merensky and UG2 Reefs northwards, towards the boundary of the TML, Zebediela and/or Welgevonden/Southern Fault systems,. Key outcomes of the study are:

1. Construction of a representative, fully-implicit, dynamic geological model of the Merensky and UG2 Reefs over the Rustenburg Layered Series of the BC. This bodes well for similar "proof-of-concept" studies over similarly large terranes, and it is apparent that implicit 3D geomodelling over such a large

area is eminently possible, although modelling artefacts and limitations always require review and management to remain representative and realistic;

2. Identification and analysis of subtle trends, patterns and domains in model outputs, which may not have been apparent from numerous, more focussed or isolated studies. This study produced implicitly-modelled surfaces that were amenable to review and trend analysis. These trends include:
    a. Absence of the Eastern Limb west of Messina Mine;
    b. North-upwards steeping of modelled reefs, with apparent uplift in proximity to the Stofpoort/Wonderkop fault systems, reflecting impingement and probably due to the 10 km uplift to the north, interpreted by Good and de Wit (1997);
    c. Relatively shallow-dipping Merensky and UG2 Reef geometries east of the Crocodile River Fault, with Merensky and UG2 Reefs appearing to shallow eastwards, with an overall homogenous reef dip over this area;
    d. Zone of apparently low and constant inter-reef separation, approximately 50 km SW of the Dennilton Dome;
    e. In the area between the southern terminations of the Eastern and Western limbs, moderate reef depths, low inter-reef separations and moderate reef dips.
    f. The coincidence of deep reef and the overlying presence of the Lebowa Granite Suite; although a direct spatial relationship between reef depth and overlying granites has not been documented previously in the literature.
3. Identification of areas or features that add to the current understanding of the BC's kinematic history and cumulative deformation. In the area between the southern terminations of the Eastern and Western limbs, moderate reef depths, inter-reef separations and moderate reef dips suggesting that reefs in this area are likely to have been only moderately deformed during southerly vergence. This coincides with observations and interpretations proposed by Basson (2019), that the offset between the Southern Limb and the Western Limb was right-lateral, accommodating an apparent 35° rotation anticlockwise, with the initial BC body behaving in a ductile manner at depth, while strain accommodation near-surface was brittle or brittle-ductile, as a series of "relay faults".

Modelling procedures developed for this project were designed with iterative model construction in mind. The model may be updated rapidly upon the incorporation of additional datasets and further data acquisition from various mines and exploration programs will greatly improve modelling results. This model should be seen as an initial data repository, with periodic and dynamic updates to incorporate additional data sets as these become available.

Resultant geometries and interpretations are dependent on data distribution and quality, which is true of any 3D model. However, the exact position of additional data will have a significant impact on modelling results and such data, be it geophysical or direct, and this is likely to have a large impact on the centre of the geological model, where available data are currently almost non-existent. A series of 2D seismic sections, which may have already been obtained by mining and exploration companies, would be particularly helpful. As new geological and remote sensing data become available, their judicious incorporation will continue to influence our understanding on the geometry and kinematic history of the complex.

Further fault activation, or fault domain delineation, is suggested in future modelling iterations, data-permitting. This, in conjunction with more local or mine-scale comparisons, would provide increasingly more robust outputs that should be more amenable to a greater surety of interpretation, as the local, higher-resolution data will have a greater impact on model results within smaller fault domains, wherein information is currently “diluted”. Effectively constraining the central zone, between the EL and WL, will prove challenging, given the paucity of data.

The results of this study have the potential to markedly improve our understanding of the overall structural and kinematic history of the Bushveld Complex. This understanding, with the further contextualization of relatively accurate regional scale Merensky and UG2 reef contours, have the potential to significantly improve future mineral exploration campaigns with regards to targeting of potential unexplored or unidentified mineralization.

9 References

Armit, R.J., Ailleres, L., Baines, A.G. and Betts, P.G. (2010). Understanding the limitations provided by unconstrained potential-field inversions on 3D models: a case study from the Mount Painter Inlier, SA. Geo-Computing 2010 Conference, Brisbane, AIG Bulletin No. 49.

Ashwal, L.D., Webb, S.J. and Knoper, M.W. (2005a). Magmatic stratigraphy in the Bushveld northern lobe: continuous geophysical and mineralogical data from the 2950 m Bellevue drillcore. South African Journal of Geology, 108, pp. 199-132.

Ashwal, L.D., Webb, S.J. and Knoper, M.W. (2005b). Physical and mineralogical properties of Bushveld rocks: magnetic susceptibility, density and mineral chemistry profiles in the 2950 m Bellevue drillcore, Northern Lobe. South African Journal of Geology 108, pp. 199-232.

Bamisaiye, O.A., Eriksson, P.g., Van Rooy, J.L., Brynard, H.M., Foya, S., Billay, A.Y., Nxumalo, V. (2017). Subsurface mapping of Rustenburg Layered Suite (RLS), Bushveld Complex, South Africa: Inferred structural features using borehole data and spatial analysis. Journal of African Earth Sciences, 132, pp. 139–167.

Basson, I.J. (2019). Cumulative deformation and original geometry of the Bushveld Complex. Tectonophysics, 750, pp. 177–202.

Bloomenthal, J. and Wyvill, B. (1997) Introduction to Implicit Surfaces. San Francisco, CA, USA: Morgan Kaufmann Publishers Inc.

Boorman, S., Boudreau, A. and Kruger, F.J. (2004). The Lower Zone-Critical Zone transition of the Bushveld Complex: A quantitative textural study. Journal of Petrology, 45, pp. 1209–1235.

Buick, I.S., Maas, R. and Gibson, R. (2001). Precise U–Pb titanite age constraints on the emplacement of the Bushveld Complex, South Africa. Journal of the Geological Society, 158, pp. 3–6.

Cameron, E.N. (1977). Chromite in the central sector of the Eastern Bushveld Complex, South Africa. American Mineralogist, 62, pp. 1082–1096.

Campbell, G. (2011). Exploration geophysics of the Bushveld Complex in South Africa. The Leading Edge, 30, pp. 622–638.

Carr, H.W. Groves, D.I. and Cawthorn, R.G. (1994). The importance of syn-magmatic deformation in the formation of the Merensky Reef potholes in the Bushveld Complex. Economic Geology, vol. 89 1994, pp. 1398-1410.

Caumon, G., Gray, G., Antoine, C., and Titeux, M. (2013). Three-Dimensional Implicit Stratigraphic Model Building From Remote Sensing Data on Tetrahedral Meshes: Theory and Application to a Regional Model of La Popa Basin, NE Mexico. IEEE Transactions on Geoscience and Remote Sensing, 51. pp 1613-1621.

Cawthorn, R.G. (1999). The platinum and palladium resources of the Bushveld Complex. South African Journal of Science, 95, pp. 481-489.

Cawthorn, R.G. and Webb, S.J. (2001). Connectivity between the Western and Eastern Limbs of the Bushveld Complex. Tectonophysics 330, pp. 195-209.

Cawthorn, R.G. and Spies, L. (2003). Plagioclase content of cyclic units in the Bushveld Complex, South Africa. Contributions to Mineralogy and Petrology, 145, pp. 47-60.

Cawthorn, R.G., Barnes, S.J., Ballhaus, C., and Malitch, K.N. (2005). Platinum-group element, chromium, and vanadium deposits in mafic and ultramafic rocks. Economic Geology, 100th Anniversary Volume. pp. 215-249.

Cawthorn, R.G. and McKenna, N. (2006). The extension of the Western Limb, Bushveld Complex (South Africa), at Cullinan Diamond Mine. Mineralogical Magazine, 70, pp. 241-256.

Cawthorn, R.G., Eales, H.V., Walraven, F., Uken, R., Watkeys, M.K. (2006). The Bushveld Complex. In: Johnson, M.R., Anhaeusser, C.R. and Thomas, R.J., (Eds). The Geology of South Africa. Geological Society of South Africa, Pretoria. pp. 261-281.

Cawthorn, R.G. (2012). The Residual or Roof Zone of the Bushveld Complex, South Africa. Journal of Petrology, 54, pp. 1875-1900.

Cheney, E. S. and Twist, D. (1991). The conformable emplacement of the Bushveld mafic rocks along a regional unconformity in the Transvaal succession of South Africa. Precambrian Research, 52, pp. 115–132.

Clarke, B.M., Uken, R. and Watkeys, M. K. (2000). Intrusion mechanisms of the southwestern Rustenburg Layered Suite as deduced from the Spruitfontein inlier. South African Journal of Geology, 103, pp. 120–127.

Clarke, B., Uken, R. and Reinhardt, J. (2009). Structural and compositional constraints on the emplacement of the Bushveld Complex, South Africa. Lithos. Elsevier B.V., 111, pp. 21–36.

Coetzee, J. and Twist, D. (1989). Disseminated tin mineralization in the roof of the Bushveld Granite Pluton at the Zaaiplaats Mine, with implications for the genesis of magmatic hydrothermal tin systems. Economic Geology, 84, pp. 1817–1834.

Cole, J., Finn, C.A. and Webb, S.J. (2013). Overview of the magnetic signatures of the palaeoproterozoic rustenburg layered suite, bushveld complex, South Africa. Precambrian Research. Elsevier B.V., 236, pp. 193–213.

Cole, J., Webb, S.J. and Finn, C.A. (2014). Gravity models of the Bushveld Complex - Have we come full circle?. Journal of African Earth Sciences. Elsevier Ltd, 92, pp. 97–118.

Coomber, S.J. (2008) Gravity modelling the Western Bushveld Complex, South Africa, using integrated geophysical data. University of the Witwatersrand, Johannesburg.

Cousins, C.A. (1959). The Structure of the Mafic Portion of the Bushveld Igneous Complex. Transactions of the Geological Society of South Africa, 1, pp. 179–201.

Cowan, J., Beatson, R., Ross, H.J., Fright, W.R., McLennan, T.J., Evans, T.R., Carr, J.C., Lane, R.G., Bright, D.V., Gillman, A.J., Oshurst, P.A., and Titley, M. (2003). Practical Implicit Geological Modelling. 5th International Mining Geology Conference.

Cowan, E. J., Spragg, K.J. and Everitt, M.R. (2011). Wireframe-Free Geological Modelling – An Oxymoron or a Value Proposition?. Eighth International Mining Geology Conference , (August 2011), pp. 22–24.

Davis, M.D., Wilson, A.H., and van der Merwe, A.J. (2007). The use of density as a stratigraphic and correlative tool for the Bushveld Complex, South Africa. Proceedings of Exploration 07: Fifth Decennial International Conference on Mineral Exploration. Milkereit, B. (Ed.) Decennial Mineral Exploration Conferences, Toronto. 1193-1197.

Davis, M.D., Wilson, A.H., van der Merwe, A.J., 2007. The use of density as a stratigraphic and correlative tool for the Bushveld Complex, South Africa. In: Milkereit, B. (Ed.), Proceedings of Exploration 07: Fifth Decennial International Conference on Mineral Exploration. Decennial Mineral Exploration Conferences, Torontopp. 1193–

1197

Deemer, S. and Hurich, C. (1997). Seismic image of the basal portion of the Bjerkreim-Sokndal layered intrusion. Geology, 25, pp. 1107–1110.

Driscoll, T.A. and Heryudono, A.R.H. (2007). Adaptive residual subsampling methods for radial basis function interpolation and collocation problems. Computers and Mathematics with Applications, 53, pp. 927–939.

Du Plessis, A. and Kleywegt, R. J. (1987). A dipping sheet model for the mafic lobes of the Bushveld Complex (South Africa). South African Journal of Geology, 90, pp. 1–6.

Du Plessis, C.P. and Walraven, F. (1990). The tectonic setting of the Bushveld Complex in Southern Africa, Part 1. Structural deformation and distribution. Tectonophysics, 179, pp. 305–319.

Eales, H.V., Botha, W.J., Hattingh, P.J., de Klerk, W.J., Maier, W.D. and Odgers, A.T.R. (1993). The mafic rocks of the Bushveld Complex: a review of emplacement and crystallization history, and mineralization, in the light of recent data. Journal of African Earth Sciences (and the Middle East) 16, 121-142.

Eales, H.V. and Cawthorn, R.G. (1996). The Bushveld Complex. Developments in Petrology, 15, pp. 181–229.

Eriksson, P.G. and Reczko, B.F.F. (1995). The sedimentary and tectonic setting of the Transvaal Supergroup floor rocks to the Bushveld complex. Journal of African Earth Sciences, 21(4), pp. 487–504.

Eales, H.V. and Costin, G. (2012). Crustally contaminated komatiite: Primary source of the chromitites and marginal, Lower, and Critical zone magmas in a staging chamber beneath the Bushveld Complex. Economic Geology, 107, pp. 645–665.

Ferré, E.C., Wilson, J. and Gleizes, G. (1999). Magnetic susceptibility and AMS of the Bushveld alkaline granites, South Africa. Tectonophysics, 307, pp. 113–133.

Finn, C.A., Bedrosian, P.A. Cole, J.C., Khoza, T.D. Webb, S.J. (2015). Mapping the 3D extent of the Northern Lobe of the Bushveld layered mafic intrusion from geophysical data. Precambrian Research Volume 268, 279-294. – Large scale geophysics

Fornberg, B., Driscoll, T.A., Wright, G. and Charles, R. (2002). Observations on the behavior of radial basis function approximations near boundaries. Computers and Mathematics with Applications, 43, pp. 473–490.

Funtowicz, S.O. and Ravetz, J.R. (1990) Uncertainty and Quality in Science for Policy. Kluwer Academic Publishers.

Gerya, T.V., Uken, R., Reinhardt, J., Watkeys, M.K., Maresch, W.V., and Clarke, B.M. (2004). “Cold” diapirs triggered by intrusion of the Bushveld Complex: Insight from two-dimensional numerical modeling, in Whitney, D.L, Teyssier, C., and Siddoway, C.S., Gneiss domes in orogeny: Boulder, Colorado, Geological Society of America Special Paper 380, p. 117-127.

Gibson, R.L., Courtnage, P. M. and Charlesworth, E. G. (1999). Bedding-parallel shearing and related deformation in the lower Transvaal Supergroup north of the Johannesburg Dome, South Africa. South African Journal of Geology, 102, pp. 99–108.

Good, N. and De Wit, M. J. (1997). The Thabazimbi-Murchison Lineament of the Kaapvaal Craton, South Africa: 2700 Ma of episodic deformation. Journal of the Geological Society, 154, pp. 93–97.

Gruenewaldt, G. von (1979). Gomplex ’ of the Bushveld Concepts of Some Recent a Review To Sulfide Reference Wnn Particular. Canadian Mineralogist, 17, pp. 233–256.

Gupta, K.H.V. and Sutcliffe, R. (1990). Mafic-ultrafic intrusives and their gravity field: Lac des Iles area, northern Ontario. Geological Society of America Bulletin - GEOL SOC AMER BULL, 102, pp. 1471–1483.

Hall, A.L. (1932). The Bushveld igneous complex of the central Transvaal. Pretoria : Dept. of Mines and Industries.

Hartzer, F.J. (1995). Constraints on the Origin of Layered Instrusions: The Bushveld Complex, South Africa Transvaal Supergroup inliers: geology, tectonic development and relationship with the Bushveld complex, South Africa. Journal of African Earth Sciences, 21, pp. 521–547.

Hattingh, P.J. (1991). The magnetic susceptibility of the mafic rocks of the Bushveld Complex. 94, pp. 132–136.

Hemant, K. (2003). Modelling and Interpretation of Global Lithospheric Magnetic Anomalies. Freien Universität Berlin.

Hillier, M., de Kemp, E. and Schetselaar, E. (2013). 3D form line construction by structural field interpolation (SFI) of geologic strike and dip observations. Journal of Structural Geology, 51, pp. 167–179.

Hulbert, L. J. (1982). Nickel , Copper , and Platinum Mineralization in the Lower Zone of the Bushveld Complex , South of Potgietersrus. Geology, 77, pp. 1296–1306.

Hunter, D.R., 1975. The Regional Geologic Setting of the Bushveld Complex (An adjunct to the provisional tectonic map of the Bushveld Complex). Economic Geology Research Unit, University of the Witwatersrand, pp. 18.

Hunter, D.R., 1976. Some enigmas of the Bushveld Complex. Econ. Geol. 71, 229–248. Hunter, D.R., Hamilton, P.I., 1978. The Bushveld Complex. In: Tarling, D.H. (Ed.), Evolution of the Earth's Crust. Academic Press, London, pp. 103–107.

Hunter, D.R., Reid, D.L., 1987. Mafic dyke swarms in southern Africa. In: Hall, H.C., Fahrig, W.F. (Eds.), Mafic Dyke Swarms Volume. Geological Association of Canada Special

Jessel, M., Aillères, L.,de Kemp, E., Lindsay, M., Wellmann, F., Hillier, M., Laurent G., Carmichael, T. and Martin R. (2014). Next Gen eration Three-Dimensional Geologic Modeling and Inversion. Building Exploration Capability for the 21st Century, pp. 261–272.

Jones, M. Q. W. (2017). Thermophysical properties of rocks from the Bushveld Complex. Journal of the Southern African Institute of Mining and Metallurgy, 115, pp. 1–14.

Karinen, T. (2010). The koillismaa intrusion northeastern finland - Evidence for pge reef forming processes in the layered series. Bulletin of the Geological Survey of Finland, (404), pp. 1–176.

Kinnaird, J.A., Yudovskaya, M., McCreesh, M., Huthmann, F., Botha, T.J., 2017. The Waterberg platinum group element deposit: Atypical mineralization in mafic-ultra- mafic rocks of the Bushveld Complex, South Africa. Econ. Geol. 112, 1367–1394.

Kruger, F. J. (2005). Filling the Bushveld Complex magma chamber: lateral expansion, roof and floor interaction, magmatic unconformities, and the formation of giant chromitite, PGE and Ti-V-magnetitite deposits. Mineralium Deposita, 40, pp. 451–472.

Ledwaba, L., Dingoko, O., Cole, P., Havenga, M., 2009. Compilation of survey specifi- cations for all the old regional airborne geophysical surveys conducted over South Africa. In: Council for Geoscience Report, pp. 40

Lenhardt, N. and Eriksson, P.G. (2012). Volcanism of the Palaeoproterozoic Bushveld Large Igneous Province: The Rooiberg Group, Kaapvaal Craton, South Africa. Precambrian Research. Elsevier B.V., 214–215, pp. 82–94.

Letts, S., Torsvik, T.H., Webb, S.J., Ashwal, L.D., Eide, E.A. and Chunnett, G. (2005). Palaeomagnetism and 40Ar/39Ar geochronology of mafic dykes from the eastern Bushveld Complex (South Africa). Geophysical Journal International, 162, 36-48.

Letts, S., Torsvik, T.H., Webb, S., and Ashwal, L.D. (2009). Palaeomagnetism of the 2054 Ma Bushveld Complex (South Africa): Implications for emplacement and cooling. Geophysical Journal International, 179, 850-872.

Letts, S., Torsvik, T.H., Webb, S.J. and Ashwal, L.D. (2011). New Palaeoproterozoic palaeomagnetic data from the Kaapvaal Craton, South Africa. Geological Society, London, Special Publications, 357, 9-26.

Li, C., Maier, W.D. and De Waal, S. A. (2001). The role of magma mixing in the genesis of PGE mineralization in the Bushveld complex: Thermodynamic calculations and new interpretations. Economic Geology, 96, pp. 653–662.

Lindsay, M.D., Ailleres, L., Jessel, M.W., de Kemp, E.A and Betts, P.G. (2012). Locating and quantifying geological uncertainty in three-dimensional models: Analysis of the Gippsland Basin, southeastern Australia. Tectonophysics. Elsevier B.V., 546–547, pp. 10–27.

Maier, W.D. and De Waal, S.A. (2001). The role of magma mixing in the genesis of PGE mineralization in the Bushveld complex: Thermodynamic calculations and new interpretations. Economic Geology, 96, pp. 653–662.

Mahammad, S.S. and Ramakrishnan, R. (2003). Map India 2003 Image Processing & Interpretation GeoTIFF - A standard image file format for GIS applications Map India 2003 Image Processing & Interpretation. Map India Conference.

Masse, P. and Laurent, O. (2016). Geological exploration of Angola from Sumbe to Namibe: A review at the frontier between geology, natural resources and the history of geology. Comptes Rendus - Geoscience. Academie des sciences, 348, pp. 80–88.

Mathez, E.A. and Mey, J.L. (2005). Character of the UG2 chromitite and host rocks and petrogenesis of its pegmatoidal footwall, northeastern Bushveld Complex. Economic Geology, 100, pp. 1617–1630.

McCall, M.-J. (2016) Mineralogical and geochemical variations in the UG2 reef at Booysendal and Zondereinde mines , with implications for beneficiation of PGM. Stellenbosch University.

McKenna, N. (1999) Petrography and Geochemistry of the Bushveld Complex in the Cullinan-Rayton Area, South Africa. University of the Witwatersrand.

Meyer, R. and de Beer, J.H. (1987). Structure of the Bushveld Complex from resistivity measurements. Nature. Nature Publishing Group, 325, p. 610.

Molyneux, T.G. and Klinkert, P.S. (1978). A structural interpretation of part of the eastern mafic lobe of the Bushveld Complex and its surrounds. Transactions of the Geological Society of South Africa, 81, pp. 359–368.

Molyneux, T.G., 1974. A geological investigation of the Bushveld Complex in Sekhukhuneland and part of the Steelpoort valley. Trans. Geol. Soc. S. Afr. 77, 329–338.

Molyneux, T.G., 2008. Compilation on a scale of 1:50,000 of the Geology of the Eastern Compartment of the Bushveld Complex. Bushveld Intelligence Center, Dept of Geology, University of Pretoria, Pretoria.

Mondal, S.K. and Mathez, E.A. (2007). Origin of the UG2 chromitite layer, Bushveld Complex. Journal of Petrology, 48, pp. 495–510.

Naldrett, T., Jinnaird, J., Wilson, A. and Chunnett, G. (2008). Concentration of PGE in the Earth's Crust with Special Reference to the Bushveld Complex. Earth Science Frontiers. China University of Geosciences (Beijing) and Peking University, 15, pp. 264–297.

Rezaie, M., Moradzadeh, A., Kalate, A., Aghajani, H., Kahoo, A., and Moazam, S. (2017). 3D modelling of Trompsburg Complex (in South Africa) using 3D focusing inversion of gravity data. Journal of African Earth Sciences, 130, 1-7.

Schouwstra, R.P., Kinloch, E.D. and Lee, C.A. (2000). A Short Geological Review of the Bushveld Complex. Platinum Metals Review, 44, pp. 33–39.

Seabrook, C.L., Cawthorn, R.G. and Kruger, F.J. (2005). The Merensky reef, Bushveld Complex: Mixing of minerals not mixing of magmas. Economic Geology, 100, pp. 1191–1206.

Sharpe, M.R. and Snyman, J.A. (1980). A model for the emplacement of the eastern compartmes of the bushveld complex. 65, pp. 85–110.

Stoch, B., Anthonissen, C.J., McCall, M-J., Basson, I.J., Deacon, J., Cloete, E., Botha, J., Britz, J., Strydom, M., Nel,

D. and Bester, M. (2017). 3D implicit modeling of the Sishen Mine: new resolution of the geometry and origin of Fe mineralization. Mineralium Deposita, 53, 835–853.

du Toit, A.L. (1954) The geology of South Africa. Edited by Boyd and Oliver. Edinburgh, U.K.

Uken, R. (1998) The geology and structure of the Bushveld Complex metamorphic aureole in the Olifants River area by. University ofNatal, Durban, South Africa.

Uken, R. and Watkeys, M.K. (1997). Diapirism initiated by the Bushveld Complex , South Africa. Geology, (8), pp. 723–726.

Vermaak, C.F. and Hendriks, L.P. (1976). A review of the mineralogy of the Merensky Reef, with specific reference to new data on the precious metal mineralogy. Economic Geology, 71, p. 1244.

Viljoen, M.J. (1999). The nature and origin of the Merensky Reef of the western Bushveld Complex based on geological facies and geophysical data. South African Journal of Geology, 102, pp. 221–239.

Viljoen, M.J. and Schurmann, L.W. (1998). Platinum-group metals. in Wilson, M. G. C. and Annhaeusser, C. . (eds) The Mineral Resources of South Africa. 6th edn. Council for Geoscience, pp. 532–568.

Vollgger, S.A., Saumur, B-M., Cowan, J., & Cruden, A.R. (2012). Implicit 3D geological modelling applied to structurally complex mineral deposits - it's all about geometry. Abstract from International Geological Congress, 2012, Brisbane, Australia.

Vollgger, S., Cruden, A., Ailleres, L., and Cowan, J. (2015). Regional dome evolution and its control on ore-grade distribution: Insights from 3D implicit modelling of the Navachab gold deposit, Namibia. Ore Geology Reviews. 69. 268-284.

Vollgger, S.A., Cruden, A.R. and Cowan, J. (2013). 3D implicit geological modelling of a gold deposit from a structural geologist's point of view. Proceedings to 12th SGA Biennial Meeting, (March 2015).

Voordouw, R., Gutzmer, J. and Beukes, N. (2010). Zoning of platinum group mineral assemblages in the UG2 chromitite determined through in situ SEM-EDS-based image analysis. Mineralium Deposita, 45, pp. 147–159.

Walraven, F. and Hattingh, E. (1993). Geochronology of the Nebo Granite, Bushveld Complex. South African Journal of Geology, 96, pp 31 – 41.

Walraven, F., 1989. The Geology of the Pilgrims Rest Area. Explanation to Sheet 2430 (Pilgrims Rest). South Africa. pp. 1180.

Walraven, F. (1997). Geochronology of the Rooiberg group, Transvaal supergroup, South Africa. Witwatersrand University Press

Webb, S.J., Cawthorn, R.G., Nguuri, T., and James, D. (2004). Gravity modeling Bushveld complex connectivity supported by Southern African Seismic Experiment results. South African Journal of Geology, 107, pp. 207–218.

Webb, S.J., Ashwal, L.D. and Cawthorn, R.G. (2011). Continuity between eastern and western Bushveld Complex, South Africa, confirmed by xenoliths from kimberlite. Contributions to Mineralogy and Petrology, 162(1), pp. 101–107.

Williams, N., de Wet, B., Kekana, S., Nielsen, S., and Broughton, D. (2016). Applying Advanced Gravity and Magnetic Inversion Methods to Expand the Platreef PGE-Ni-Cu Resource in the Bushveld Complex. ASEG Extended Abstracts.

Zeh, A. Ovtcharova, M., Wilson, A.H. and Schaltegger, U. (2015). The Bushveld Complex was emplaced and cooled in less than one million years - results of zirconology, and geotectonic implications. Earth and Planetary Science Letters.

10 Appendix

10.1 Appendix 1: Council for Geosciences Drillhole Collars

CGS Drillhole ID	East	North	Elevation	Maximum Depth	ID Number	SAG	Company Name
B3888	55618.13494	-2913497.687	1600	412.3944	4201896	90102318	Northwestern Transvaal Base Metals
RY1	-148783.0324	-2730440.794	925	1512.11	4212179	90262611	
B34398 2	-176159.8697	-2742045.148	977	1527	2005716	0	
B5226	-176905.3118	-2743406.706	982	631.8504	2005669	90004870	Anglo American Prospecting Services
B32162/3	-160760.1745	-2743495.515	923.28	1941.39	2005595	90004872	
B32162/1	-163464.719	-2743684.167	946.58	1482.09	2005593	90004872	
B32162	-162453.2681	-2743891.451	936.4	1751.07	2005592	90004872	
B32162/2	-162690.634	-2745000.381	946.58	2039.45	2005594	90004872	
B32162/4	-160772.8867	-2745028.877	937.48	2287	2005596	90004872	
B32163 2	-165540.1137	-2746776.754	975.58	1958.12	2005599	90004872	
B32163 4	-167396.6079	-2746934.117	973.48	1527	2005601	90004872	
B32163 7	-164451.5971	-2747265.214	961.48	2442.7	2005604	90004872	
1357	-175679.9459	-2747830.886	975.4	127.1	2005693	90004879	Impala Platinum
B32163	-168308.0477	-2747770.837	973.88	1578	2005597	90004872	
B27834	-176389.2532	-2747901.313	985	352.5	2005683	90004879	Impala Platinum
2535	-176063.0674	-2747971.567	982	341.97	2005707	90004877	
2536	-175847.0576	-2748033.431	975.5	279	2005708	90004877	
2530	-176251.7978	-2748064.377	980	416.2	2005709	90004877	
B28229 1	-176049.0318	-2748246.493	979.9	246.2	2005685	90004879	Impala Platinum
2471	-175857.6619	-2748333.73	981	399.78	2005675	90004877	
B32163 5	-167478.175	-2748365.135	977.08	1871.44	2005602	90004872	
2404	-176060.3691	-2748496.779	985	453.59	2005681	90004877	
B32163 3	-169248.7396	-2748413.907	961.28	1443.39	2005600	90004872	
2461	-176034.9225	-2748526.42	981	503.4	2005680	90004877	
B5224	-175549.4286	-2748544.313	974	293.218	2005667	90004870	Anglo American Prospecting Services
B27988	-175507.5847	-2748668.759	972.4	356.2	2005690	90004879	Impala Platinum
2544	-176357.8083	-2748681.226	982	596.4	2005710	90004877	
B32163 6	-165858.7473	-2748592.918	990.08	2337.48	2005603	90004872	
B29003	-175996.6864	-2748745.964	975.4	527.6	2005689	90004879	Impala Platinum
B28281	-175300.1844	-2748825.793	967.6	391	2005687	90004879	Impala Platinum
B28402	-175775.015	-2748852.766	972.3	401.4	2005688	90004879	Impala Platinum
B28229 2	-176394.5918	-2748901.872	983	333.8	2005686	90004879	Impala Platinum
2500	-175544.3681	-2748889.403	968	418.54	2005677	90004877	
B5225	-176163.6508	-2748958.513	980	582.168	2005668	90004870	Anglo American Prospecting Services
2522	-175923.2941	-2748974.998	972.6	579.72	2005706	90004877	
B34833	-176398.1262	-2749001.971	976	667.88	2005702	90004877	

CGS Drillhole ID	East	North	Elevation	Maximum Depth	ID Number	SAG	Company Name
2551	-175121.0315	-2749103.299	966	505.07	2005673	90004877	
2533	-176130.4154	-2749178.131	977	775.6	2005671	90004877	
2477	-175747.4546	-2749367.608	970	635	2005676	90004877	
2537	-175077.06	-2749372.782	963	584.47	2005672	90004877	
B34511 1	-176444.6315	-2749582.932	986	816.2	2005699	90004877	
B32830	-176657.6467	-2750066.288	980	1030.3	2005721	90004877	Impala Platinum
B34554	-174456.6319	-2750064.011	930	865.4	2005664	90004877	
B34511 2	-174856.5878	-2750079.884	951.7	686.08	2005700	90004877	
B34549	-176056.4603	-2750127.502	964	919.98	2005663	90004877	
B32163 1	-169177.4481	-2750034.582	975.98	1759.76	2005596	90004872	
B34089	-174825.4061	-2750159.464	960	1100.87	2005715	90004877	
B29510	-175184.3251	-2750244.768	955.5	819.5	2005691	90004879	Impala Platinum
B32164	-167582.5703	-2750155.647	982.68	2435.21	2005544	90004872	
2521	-175540.1625	-2750540.127	945	845	2005670	90004877	
2212	-176021.033	-2750837.322	962.9	966.3	2005703	90004877	Genmi Platinum
B34213	-175570.4012	-2750865.726	960	1140.3	2005718	0	
B32852	-176213.589	-2751010.229	962	1084.3	2005720	90004877	Impala Platinum
B34596	-175153.1648	-2751004.671	952	986.21	2005665	90004877	
B34398 1	-176841.9949	-2751139.51	979	1260.28	2005717	0	
2287	-176197.8609	-2751400.185	970	1476	2005678	90004877	Genmi Platinum
B32031	-175895.0408	-2751425.755	962.78	1170	2005694	90004872	
2262	-173720.754	-2751463.874	969	1320.09	2005704	90004877	Genmi Platinum
B34503	-176221.9958	-2751800.732	970	1618.6	2005712	90004877	Maatskappy Genov Ltd
2408	-175486.5257	-2752490.268	960	1601.04	2005711	90004877	
B32031 MG7	-175368.0748	-2752491.941	965.48	1551.29	2005697	0	
B34369	-176715.5354	-2752938.522	968	1954	2005719	90004877	
B32033 KV1	-173676.721	-2752997.254	978.98	1725.3	2005610	90004872	
B32031 MG8	-176387.6231	-2753071.673	960.68	2002.92	2005698	0	
B32033 KV2	-174777.2713	-2753567.868	975.38	1977.66	2005611	0	
B34459	-174685.311	-2753569.019	975	2586.1	2005616	90004877	
B33051	-173159.4301	-2754942.254	985	2563.32	2005614	90004877	Impala Platinum
B1751	69538.10599	-2789958.058	1246	76.2	2018107	90004587	Anglo American Prospecting Service
B1752	70228.10393	-2790578.056	1315	91.44	2018108	90004587	Anglo American Prospecting Service
BH3413	-140503.4517	-2796395.737	1192.9	126.24	0	0	
B34597	-120394.6745	-2824140.477	1136.7	490.53	2017619	90004530	
B34576	-120076.582	-2825564.988	1121.9	550	2017618	90004530	
B34555	-119861.4029	-2826843.214	1111	424	2017617	90004530	
B34547	-119673.0498	-2828252.369	1113.1	444.5	2017616	90004530	
ZS021	-151514.6708	-2833250.18	1123.1	1413.94	0	0	
BH1995	-108635.3479	-2834112.64	1228.4	1586.91	0	0	
SL10	-155323.1673	-2834951.022	1121.19	1834.86	0	0	
SL08	-153777.7624	-2834943.682	1147.51	1950	0	0	

CGS Drillhole ID	East	North	Elevation	Maximum Depth	ID Number	SAG	Company Name
SL11	-149046.1806	-2834887.492	1104.84	1963.44	0	0	
SL09	-151291.1941	-2834925.838	1102.76	1963.44	0	0	
BH1990	-110112.8158	-2834819.145	1186.4	1440.15	0	0	
SL06	-156372.8824	-2835648.821	1106.71	1890	0	0	
SL13	-153676.9871	-2835757.297	1127.22	1825.44	0	0	
SL12	-155175.6306	-2835821.149	1113.83	1740.36	0	0	
SL19	-152756.3839	-2835903.747	1120.64	1766.32	0	0	
KRE2	-104006.2056	-2835371.255	1235	784.1	0	0	
B34399	-106213.8846	-2835544.604	1215.5	920.5	2017447	90004530	
SL18	-154131.5288	-2836276.012	1128.43	1729.59	0	0	
SL01	-156062.4102	-2836584.447	1123.39	1642.9	0	0	
SL04	-151265.2543	-2836524.047	1107.2	1693.59	0	0	
SL16	-152065.0801	-2836543.658	1104.13	1736.52	0	0	
SL02	-152861.2513	-2836601.449	1118.21	1774.01	0	0	
SL03	-154507.3712	-2836644.975	1131.03	1696.39	0	0	
SL05	-148206.0108	-2836592.718	1113.9	1715.38	0	0	
SL17	-155767.1155	-2837111.742	1128.23	1600.17	0	0	
B32034 SK1	-156926.473	-2837151.643	1122.2	1566	2051251	90050950	
SL15	-154248.4992	-2837289.04	1135.46	1618.54	0	0	
SL14	-152029.9577	-2837262.271	1110.17	1696.36	0	0	
B32034 SK2	-150294.7968	-2837303.466	1116.1	1619.89	2051273	90050950	
SL07	-153648.6686	-2837360.23	1139	1653.4	0	0	
ZS042	-155254.1473	-2837385.352	1129	1556.58	0	0	
SIE1	-106974.3385	-2836846.27	1225	380.84	2017444	90004534	
ZS48	-152460.642	-2837663.853	1116.63	1617.62	0	0	
ZS048	-152460.642	-2837663.853	1116.63	1617.62	0	0	
ZS039	-151237.7762	-2838115.979	1115.66	1660.39	0	0	
ZS041	-153647.4714	-2838159.911	1130.42	1531.59	0	0	
ZS040	-152029.9823	-2838153.248	1112.64	1570	0	0	
ZS050	-152400.2134	-2838607.068	1116.89	1489	0	0	
ZS038	-151080.4476	-2838774.782	1121.79	1501.39	0	0	
BH1936	-153137.6545	-2839001.259	1118.065	1379.26	0	0	
ZS028	-150567.9802	-2839315.694	1128.58	1414.89	0	0	
B5849	-9656.670162	-2598148.573	1010	145	2005020	90004241	U.C. Prospecting
B5848	-9591.670283	-2600343.568	1009	165.7	0	0	U.C. Prospecting
794	-9271.671048	-2602498.562	1012	213.2	2005051	90004241	
B5850	-9281.671008	-2603308.56	1010	265	0	90004241	U.C. Prospecting
B34531 MDH31	111362.704	-2719969.886	988	227.53	2011582	90004369	
B29305 M18	109662.6641	-2719955.199	973	156.13	2011595	90004373	
B20418	111521.0249	-2720087.203	995	169.6	2011571	90004368	
B20414	110374.4959	-2720180.568	970	316.45	2011567	90004368	
B5045	110012.2568	-2720675.381	979	156.97	2011586	90004371	
B20409	111832.4993	-2721021.871	1007	205.2	2011562	90004368	

CGS Drillhole ID	East	North	Elevation	Maximum Depth	ID Number	SAG	Company Name
B30093	109921.5973	-2721064.121	988	517.03	2011594	90004366	
B20415	110292.651	-2721339.551	990	318.1	2011568	90004368	
B27596 MDH28	112751.9298	-2721415.288	1008	76.8	2011580	90004368	
B20416	111499.382	-2721577.118	970	291.55	2011569	90004368	
B29305 M16	110307.9872	-2722004.873	999	111.94	2011593	90004373	
B20408	112262.8735	-2722033.281	977	136.53	2011561	90004368	
B19425	110457.6145	-2722032.051	994	458.2	2011588	90004372	
B5047	114156.9683	-2722460.874	1011	339.85	2011556	90004368	
B30093 MS35	112672.0242	-2722784.347	959	44.47	2011601	90004366	
B5050	110212.0927	-2722753.59	1000	495	2011585	90004370	
B30093 MS20	112871.9414	-2722792.253	960	23.3	2011599	90004366	
B30093 MS30	112695.8601	-2722864.706	958	44.38	2011600	90004366	
B30093 MS40	112620.8639	-2722863.616	957	60.78	2011602	90004366	
B30093 MS60	112545.7225	-2722872.525	957	73.23	2011604	90004366	
B30093 MS65	112470.2903	-2722901.433	959	77.68	2011605	90004374	
B20410	112366.1526	-2723184.965	945	207.43	2011563	90004368	
B29305 M13	110864.8564	-2723258.153	980	80.72	2011590	90004373	
B29024	110853.0235	-2723728.052	995	117.55	2011592	90004373	
B29256	110942.7831	-2724089.412	1003	113.2	2011591	90004373	
B5049	113793.0889	-2716179.548	1075	415.63	2011557	90004368	
B27596 MDH21	113462.2301	-2716579.816	1060	443.21	2011573	90004368	
B27596 MDH29	114244.8692	-2717096.253	1305	473.4	2011581	90004368	
B27596 MDH20	113221.3557	-2717671.5	1035	417.2	2011572	90004368	
B29305 M21	109265.3525	-2717699.109	947	96.68	2011598	90004373	
B27596 MDH23	111966.7041	-2717978.345	979	562.05	2011575	90004368	
B5044	111865.9114	-2718031.891	977	37.49	0	0	
B30093 MN20	111973.0756	-2718228.476	985	35.55	2011606	90004366	
B30093 MN30	111877.0649	-2718297.094	987	40	2011607	90004366	
B30093 MN60	110752.0574	-2718285.767	980	65.03	2011609	90004366	
B20406	110825.3113	-2718406.848	950	155.4	2011559	90004368	
B27596 MDH22	113035.1177	-2718443.922	1025	393.45	2011574	90004368	
B27596 MDH25	112131.3178	-2718695.846	1020	99.95	2011577	90004368	
B29305 M19	109453.8669	-2718837.007	962	157.69	2011596	90004373	
B20412	110059.2542	-2719160.841	950	411.45	2011565	90004368	
B20407	110973.6169	-2719214.122	966	344.7	2011560	90004368	
B20413	110618.6384	-2719208.968	959	291.21	2011566	90004368	
B24155	109691.6555	-2719680.581	969	491	2011589	90004372	
B13498	-12011.66316	-2643923.456	1094	413.8	2005087	90004182	U.C. Prospecting
B32665 54-1	-4196.683088	-2694948.32	1080	226.64	2006335	90004729	Rio Tinto Exploration
B32665 54-2	-4271.682884	-2695173.319	1080	149.77	2006336	90004729	Rio Tinto Exploration
BH3231	56850.14211	-2793263.047	1098	99	0	0	
BH3225	57176.14108	-2794225.044	1144	121.6	0	0	
BH3221	57318.14064	-2794530.043	1200	207	0	0	

CGS Drillhole ID	East	North	Elevation	Maximum Depth	ID Number	SAG	Company Name
BH3229	57329.14056	-2795025.042	1183	239.8	0	0	
BH2945	62678.12515	-2795073.042	1180	133.95	0	0	
BH3413	60973.12998	-2795803.04	1192	126.24	0	0	
EST018	115066.5197	-2735598.645	829.5220454	900			
EST019	113917.8981	-2734744.357	864.9209214	900			
NVT005	111261.7107	-2736122.703	922.4880666	900			
NVT002	111197.1008	-2735419.173	905.2326769	900			
TRP48	109555.4805	-2761358.142	1021.061104	900			
TRP64	108814.6457	-2762621.53	1013.084898	900			
BD10D0	101347.9001	-2799205.038	1838.477873	900			
BD08D0	101675.9841	-2798824.038	1838.344285	900			
TRP10	109948.267	-2757564.26	1200.462739	900			
BD09D0	101019.8161	-2799923.648	1835.253737	900			
BD11D0	102046.4015	-2797998.536	1819.138726	900			
TRP21	109626.0309	-2759088.35	1186.905951	900			
TRP31	109244.5945	-2760088.14	1229.845984	900			
TRP17	109695.7035	-2758626.769	1263.297542	900			
TRP25	109264.4383	-2759532.513	1196.255148	900			
TRP30	108854.3333	-2759962.462	1238.734306	900			
TRP16	109417.0128	-2758574.514	1354.07565	900			
TRP59	109013.0836	-2760604.078	1333.686643	900			
BD07D0	101929.9846	-2795945.365	1805.427772	900			
BD01D0	103147.0703	-2793056.109	1772.48761	900			
TRP51	108477.3013	-2761569.809	1401.333152	900			
TRP32	109734.0746	-2760081.525	1050.692042	900			
BD22D0	103760.9049	-2792103.607	1776.943915	900			
BD20D0	105750.5755	-2790526.688	1772	900			
BD16D0	107380.4121	-2789764.686	1805.3221	900			
BD24D0	104888.0322	-2789127.039	1767.398203	900			
BD18D0	106353.8268	-2788918.018	1766.388573	900			
WL201	-196061.2496	-2809271.899	1043.744201	2000			
WM01	-196571.5455	-2810592.493	1043.681553	2000			
WL206	-195565.9486	-2808763.898	1054.894316	900			
WF79	-193908.5953	-2810154.551	1038.571575	900			
WL2/13	-194551.2249	-2808748.538	1058.557913	900			
WF71	-193464.0944	-2810637.152	1021.519618	900			
RB30	-191865.6875	-2810096.847	1022.83672	900			
SD6	-191988.2069	-2809617.907	1028.197746	900			
WM02	-197321.1534	-2811585.142	1053.60933	2000			
WF01	-193235.4939	-2809640.2	1036.476124	900			
WF07	-193730.7949	-2809132.199	1052.112801	900			
WL1/03	-194065.4489	-2808237.891	1059.826826	900			
WF08	-192216.5385	-2809617.907	1031.407859	900			

CGS Drillhole ID	East	North	Elevation	Maximum Depth	ID Number	SAG	Company Name
WF23	-193502.1945	-2808776.598	1052.810443	900			
WF02	-192714.7929	-2808643.248	1054.174728	900			
WF69	-192458.8957	-2810593.746	1021.239086	2000			
WL1/07	-193564.2516	-2807741.133	1063.824771	2000			
WL203	-196080.2996	-2808287.647	1053.986826	900			
WL1/01	-192862.5497	-2807668.735	1068.468821	2000			
DT19	102613.9153	-2710936.789	848.6278294	2000			
DT24	102760.6469	-2711398.587	851.8574374	2000			
DT26	102789.7511	-2711515.004	854.1022972	2000			
DT12	102186.8329	-2709977.452	855.2939911	2000			
DT15	102674.1082	-2712040.104	864.6976089	2000			
DT21	102468.3942	-2711395.181	850.1248098	2000			
DT20	102475.0088	-2712491.219	889.5191561	2000			
DT18	102243.4979	-2711852.911	859.2274949	2000			
DT13	102073.5028	-2711193.435	855.795436	2000			
DT11	101938.3004	-2712859.652	888.8467178	2000			
DT4	104241.1061	-2711250.982	883.016358	2000			
DT2	104277.4864	-2711664.395	936.7495973	2000			
DT7	104419.7002	-2711459.342	930.42217	900			
DT17	103633.2247	-2710865.748	845.0583652	900			
DT5	103940.1419	-2711469.264	869.2994711	900			
DT6	103877.3033	-2711743.77	904.6059061	900			
DT9	103381.2085	-2710794.575	842.619302	2000			
DT8	103850.8449	-2711151.764	857.856162	2000			
DT22	103222.4582	-2710672.205	839.4375818	900			
DT1	103381.2085	-2711287.363	852.2830077	2000			
DT3	103321.6772	-2711747.077	867.4889353	2000			
DT16	103061.7235	-2711121.998	850.2050067	2000			
DT14	102676.313	-2710337.948	838.3557252	2000			
DT23	103183.9811	-2712253.193	877.9686491	2000			
DT10	102785.8948	-2711261.566	850.7387331	2000			
ARF020	-949.5412243	-2665302.535	1154.182752	900			
UMT026	-2566.307374	-2665532.776	1118.959001	2000			
UMT039	-4368.123478	-2663816.685	1113.61032	900			
UMT281	-14324.87725	-2670596.299	1542.144274	2000			
UMT217	-4111.477131	-2665049.646	1109.521516	900			
UMT172	-3893.327737	-2663873.571	1115.08186	900			
UMT280	-3586.67504	-2664000.835	1121.275025	900			
UMT249	-3865.546431	-2663738.633	1119.22818	900			
UMT145	-4181.724147	-2663612.955	1113.806323	900			
ATS046	-1348.004521	-2665260.466	1143.344775	900			
AMK081	-824.0226399	-2667802.906	1130.758606	900			
AMK051	-740.6787232	-2667993.406	1124.200019	900			

CGS Drillhole ID	East	North	Elevation	Maximum Depth	ID Number	SAG	Company Name
ARF043	-1070.985217	-2665130.291	1151.842951	900			
AMK030	-525.0428753	-2668097.917	1125.351051	900			
PLAT01	98865.33549	-2796399.656	1886.785643	2000			
PLAT02	107041.6423	-2789786.093	1788.814401	2000			
PLAT03	99987.17106	-2791658.313	1725.422383	2000			
PLAT04	105098.5384	-2789316.193	1770.297258	2000			
PLAT05	104559.1802	-2791933.48	1782.77031	2000			
PLAT06	107600.4434	-2790103.594	1790.269116	2000			
PLAT07	109852.5813	-2789422.026	1847.515228	2900			
EST012	116771.1909	-2737421.58	784.3203997	900			
BD12D0	102699.7511	-2795020.708	1781.710074	900			
BD21D0	106742.5925	-2790017.957	1768.609022	900			
BAU040	83005.66979	-2691025.506	820.7587764	2500			
BAU023	93681.92771	-2709374.643	990.4886652	2500			
BAU022	95372.50627	-2711475.059	1028.479535	2500			